



**HAL**  
open science

## Hydrogen production from biogas reforming: an overview of steam reforming, dry reforming, dual reforming, and tri-reforming of methane

Doan Pham Minh, Tan Ji Siang, Dai-Viet N. Vo, Thanh Son Phan, Cyrille Ridart, Ange Nzihou, Didier Grouset

### ► To cite this version:

Doan Pham Minh, Tan Ji Siang, Dai-Viet N. Vo, Thanh Son Phan, Cyrille Ridart, et al.. Hydrogen production from biogas reforming: an overview of steam reforming, dry reforming, dual reforming, and tri-reforming of methane. Catherine Azzaro-Pantel. Hydrogen supply chains : design, deployment and operation, Elsevier, pp.111-166, 2018, 978-0-12-811197-0. 10.1016/B978-0-12-811197-0.00004-X . hal-01876512

**HAL Id: hal-01876512**

**<https://imt-mines-albi.hal.science/hal-01876512>**

Submitted on 14 Mar 2019

**HAL** is a multi-disciplinary open access archive for the deposit and dissemination of scientific research documents, whether they are published or not. The documents may come from teaching and research institutions in France or abroad, or from public or private research centers.

L'archive ouverte pluridisciplinaire **HAL**, est destinée au dépôt et à la diffusion de documents scientifiques de niveau recherche, publiés ou non, émanant des établissements d'enseignement et de recherche français ou étrangers, des laboratoires publics ou privés.

# Hydrogen Production From Biogas Reforming: An Overview of Steam Reforming, Dry Reforming, Dual Reforming, and Tri-Reforming of Methane

Doan Pham Minh<sup>\*</sup>, Tan Ji Siang<sup>†</sup>, Dai-Viet N. Vo<sup>†</sup>, Thanh Son Phan<sup>\*</sup>, Cyrille Ridart<sup>‡</sup>, Ange Nzihou<sup>\*</sup> and Didier Grouset<sup>\*</sup>

<sup>\*</sup>Université de Toulouse, IMT Mines Albi, UMR CNRS 5302, Centre RAPSODEE, Campus Jarlard, Albi, France, <sup>†</sup>Faculty of Chemical and Natural Resources Engineering, University Malaysia Pahang, Lebuhraya Tun Razak, Gambang, Kuantan, Malaysia, <sup>‡</sup>HERA—ALBHYON, Technopole Innoprod, rue Pierre Gilles de Gennes, Albi, France

## 4.1 INTRODUCTION

The present context of climate change, fossil resource scarcity, and environmental issues imposes the development of renewable energy, such as solar, wind, geothermal, and biomass. In France, 24.5 million metric tons of oil equivalent of renewable energy were produced in 2013, which corresponds to 17.6% of the total energy amount produced this year (ADEME, 2014a). According to the last report of ADEME (agence de l'environnement et de la maîtrise de l'énergie, France) on the “lightened environmental footprint” scenario, the objective is to reduce by 17% the carbon footprint in France by 2030 (ADEME, 2014b). This energy transition dynamic is also being conducted in many other countries, such as Germany, the United Kingdom, the United States, Sweden, Norway, Switzerland, and China (IEA, 2017).

In the transport domain, much effort has been devoted to the development of electric vehicles. In parallel, the development of hydrogen vehicles is also very attractive. Up-to-date, hydrogen vehicles present some major advantages compared to electric vehicles, namely, a shorter charging time and a higher autonomy. The use of hydrogen as a clean fuel starts now, and hydrogen can become a strategic energy vector in the near future.

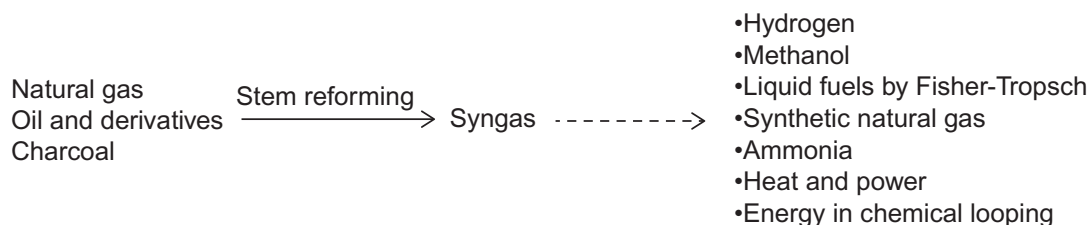
Nowadays, around 96% of hydrogen is produced from fossil resources, and particularly from natural gas, oil and derivatives, and coal. Chemicals synthesized from these fossil resources are usually obtained via synthetic gas, which is produced by steam reforming of natural gas. Details about steam reforming will be discussed later. [Scheme 4.1](#) below illustrates the most common products that can be obtained from syngas, including hydrogen, methanol, liquid fuels, synthetic natural gas (SNG), ammonia, and heat and power.

Hydrogen from water electrolysis accounts only for about 4% of total hydrogen production. Naturally, water electrolysis using electricity from renewable resources, such as solar, wind, or hydro is a promising way for green hydrogen production. However, the process still needs to be improved in order to reach the competitive cost required by the hydrogen market.

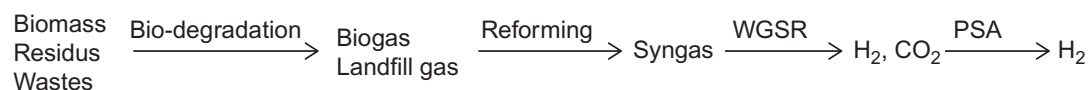
Another way to produce green hydrogen is the valorization of bioresources, such as biogas. This last one is obtained from biomass, residues, or wastes by anaerobic digestion. In general, two types of biogas are distinguished: (1) digested gas from anaerobic digester, which is commonly called biogas, and (2) landfill gas from landfill sites ([IEA, 2009](#)).

The production of hydrogen from biogas and landfill gas can be achieved via a syngas route as shown in [Scheme 4.2](#) below. Syngas is obtained from biogas or landfill gas by different reforming processes, which will be detailed later. Then a mixture of H<sub>2</sub> and CO<sub>2</sub> can be obtained from syngas by the water-gas-shift (WGS) reaction. Finally, hydrogen can be separated from the mixture with CO<sub>2</sub> by using a pressure swing adsorption (PSA) or an equivalent process.

Both biogas/landfill gas reforming and WGS are catalytic processes. The reforming step can be achieved with catalytic steam reforming process, which is already commercialized for natural gas. However, the energy balance of the steam reforming is not optimized because of a large excess of water vapor, which is required with current catalysts. Because the composition of



**SCHEME 4.1** Chemicals and energy from fossil resources via steam reforming.



**SCHEME 4.2** Main steps for the production of hydrogen from biogas or landfill gas via syngas route.

biogas/landfill gas varies as shown in [Table 4.1](#), other reforming processes can be considered, as listed below:

- Dry reforming of methane (DRM) with CO<sub>2</sub>.
- Dual reforming of methane with a mixture of CO<sub>2</sub> and H<sub>2</sub>O.
- Tri-reforming of methane (TRM) with a mixture of CO<sub>2</sub>, H<sub>2</sub>O and O<sub>2</sub>.

For a given mixture of CH<sub>4</sub> with at least one of the three oxidants (CO<sub>2</sub>, H<sub>2</sub>O, and O<sub>2</sub>), different chemical equilibriums can take place. [Table 4.2](#) summarizes the most important chemical reactions usually found in methane reforming processes. The dependence of the Gibbs free energy change per mole of reaction ( $\Delta_r G$ ) on the reaction temperature has been previously reported in the literature, and some of them have been calculated from the handbook of chemistry data. FactSage software ([Factsage, n.d.](#)) (6.3.1 version) is used for the thermodynamic equilibrium calculation of a given mixture at well-defined conditions of temperature and pressure. The calculation is based on the principle of the Gibbs free energy minimization. Standard enthalpies of reaction ( $\Delta_r H_{298}^\circ$ ) are calculated from the handbook of chemistry ([Lide, 2003–2004](#)).

**TABLE 4.1** Main Characteristics of Digested Gas and Landfill Gas in Comparison With Some Natural Gases

Compounds	Biogas	Landfill gas	Natural Gas (Danish)	Natural Gas (Dutch)
Methane (vol%)	60–70	35–65	89	81
Other hydrocarbons (vol%)	0	0	9.4	3.5
Hydrogen (vol%)	0	0–3	0	–
Carbon dioxide (vol%)	30–40	15–50	0.67	1
Nitrogen (vol%)	≈0.2	5–40	0.28	14
Oxygen (vol%)	0	0–5	0	0
Hydrogen sulfide (ppm)	0–4000	0–100	2.9	–
Ammonia (ppm)	≈100	≈5	0	–
Lower heating value (kWh/Nm <sup>3</sup> )	6.5	4.4	11.0	8.8

Adapted from IEA, 2009. IEA bioenergy, Task 37—Energy from biogas and landfill gas.

**TABLE 4.2** The Main Chemical Reactions That Occur During the Reforming of Methane With At Least One of the Following Oxidants: CO<sub>2</sub>, H<sub>2</sub>O, and O<sub>2</sub>

Reaction	$\Delta_r G$ function ( $P = 1$ bar) (kJ/mol)	$\Delta_r H_{298}^\circ$ (kJ/mol)	Equations
$\text{CH}_4 + \text{CO}_2 \rightarrow 2\text{CO} + 2\text{H}_2$	$\Delta_r G = 61,770 - 67.3 \times T$	+247	(4.1)
$2\text{CO} \rightarrow \text{C} + \text{CO}_2$	$\Delta_r G = -39,810 + 40.9 \times T$	-172	(4.2)
$\text{CO} + \text{H}_2\text{O} \rightarrow \text{CO}_2 + \text{H}_2$	$\Delta_r G = -39,802 + 37.673 \times T$	-41	(4.3)
$\text{CH}_4 \rightarrow \text{C} + 2\text{H}_2$	$\Delta_r G = 21,960 - 26.5 \times T$	+75	(4.4)
$\text{CH}_4 + \text{H}_2\text{O} \rightarrow \text{CO} + 3\text{H}_2$	$\Delta_r G = 210,359 - 233.9 \times T$	+206	(4.5)
$\text{C}_s + \text{H}_2\text{O} \rightarrow \text{CO} + \text{H}_2$	$\Delta_r G = 132,184 - 138.8 \times T$	+131	(4.6)
$2\text{CH}_4 + \text{O}_2 \rightarrow 2\text{CO} + 4\text{H}_2$	$\Delta_r G = -653.9 - 369 \times T$	-71	(4.7)
$\text{CH}_4 + 2\text{O}_2 \rightarrow \text{CO}_2 + 2\text{H}_2\text{O}$	$\Delta_r G = -803,508 + 13 \times T - 0.018 \times T^2 + 8 \times 10^{-6} \times T^3$	-802.5	(4.8)
$\text{C} + \text{O}_2 \rightarrow \text{CO}$	$\Delta_r G = -110,872 - 89.4 \times T$	-110.5	(4.9)
$\text{C} + \text{O}_2 \rightarrow \text{CO}_2$	$\Delta_r G = -393,647 - 2.5 \times T$	-393.5	(4.10)
$\text{CH}_4 + 2\text{H}_2\text{O} \rightarrow \text{CO}_2 + 4\text{H}_2$	$\Delta_r G = 170,557 - 196.29 \times T$	+165	(4.11)

(4.1) Dry reforming of methane (DRM); (4.2) Boudouard reaction; (4.3) water-gas-shift (WGS) reaction; (4.4) methane cracking; (4.5) steam reforming of methane; (4.6) steam reforming of carbon; (4.7) partial oxidation of methane; (4.8) methane combustion; (4.9) partial oxidation of carbon; (4.10) carbon combustion; and (4.11) Methane reforming with large excess of steam. All molecules are in the gas state except carbon (C), which is in the solid state.

## 4.2 METHANE REFORMING WITH STEAM (SMR) AND WITH A MIXTURE OF STEAM/CARBON DIOXIDE (DUAL-MR)

### 4.2.1 Thermodynamic Equilibrium of Steam Methane Reforming

The ideal reaction of steam methane reforming (SMR) to syngas is given in Eq. (4.5) (Table 4.2). One mole of H<sub>2</sub>O is needed to transform 1 mol of CH<sub>4</sub>. In reality, SMR is usually carried out with a large excess of steam (molar steam/carbon ratio or S/C close to 3). Fig. 4.1 shows the thermodynamic equilibrium of a CH<sub>4</sub>-H<sub>2</sub>O mixture with two different molar ratios of H<sub>2</sub>O/CH<sub>4</sub>. Only products present at significant amounts are presented. They are all in

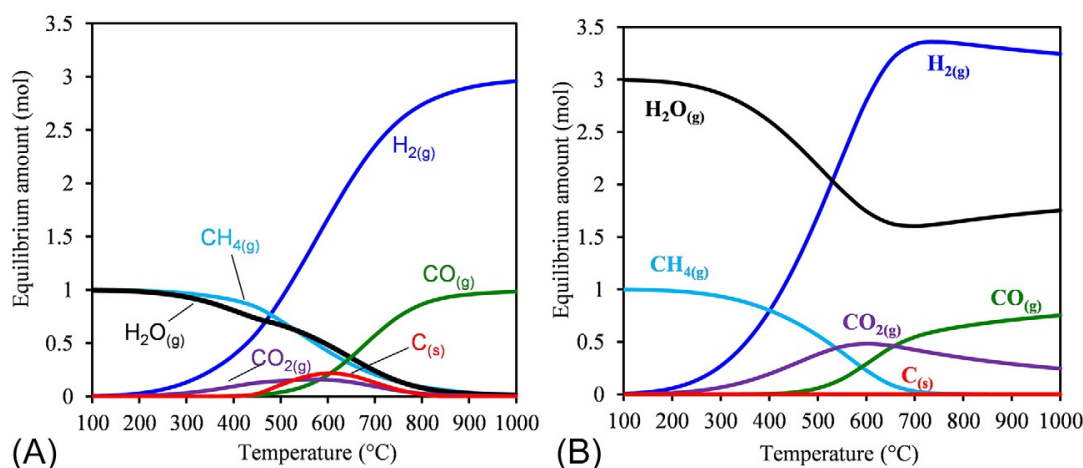


**FIG. 4.1** Thermodynamic equilibrium as a function of the temperature at atmospheric pressure of the mixture containing (A) 1 mol CH<sub>4</sub> and 1 mol H<sub>2</sub>O and (B) 1 mol CH<sub>4</sub> and 3 mol H<sub>2</sub>O.

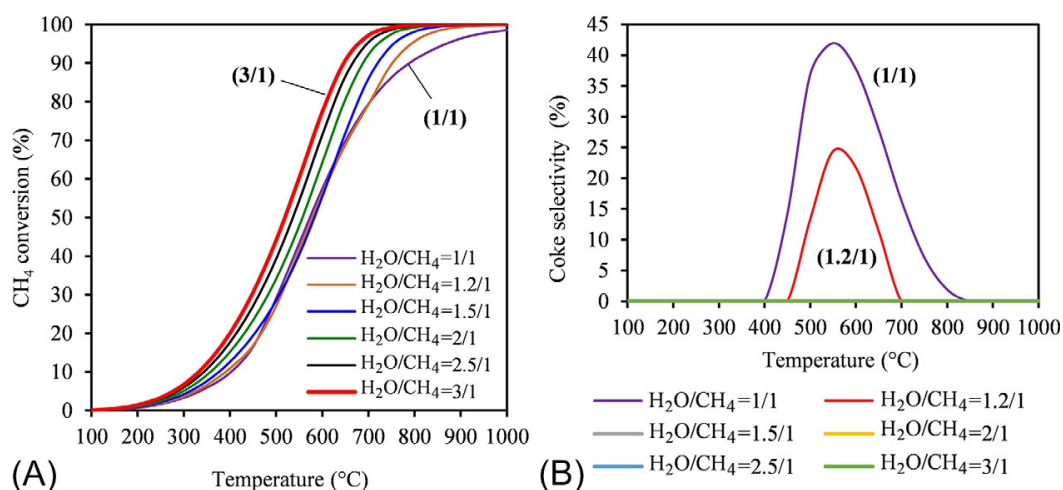
the gas state except for solid carbon (C<sub>(s)</sub>). Other hydrocarbons, such as ethylene, ethane, methanol, and acetone, can be formed in very small quantities (approximately 10<sup>-6</sup> to 10<sup>-14</sup> mol) and are not presented.

With the equimolar ratio of H<sub>2</sub>O/CH<sub>4</sub> (Fig. 4.1A), hydrogen is formed above 180°C and its content increases with the temperature. Carbon dioxide and solid carbon are formed in the temperature ranges of around 250–800°C and 450–800°C, respectively. This makes the process difficult because solid carbon formation causes catalyst deactivation, and carbon dioxide is an undesirable byproduct. Under these conditions, syngas formation is really favorable above 800°C from the thermodynamic point of view.

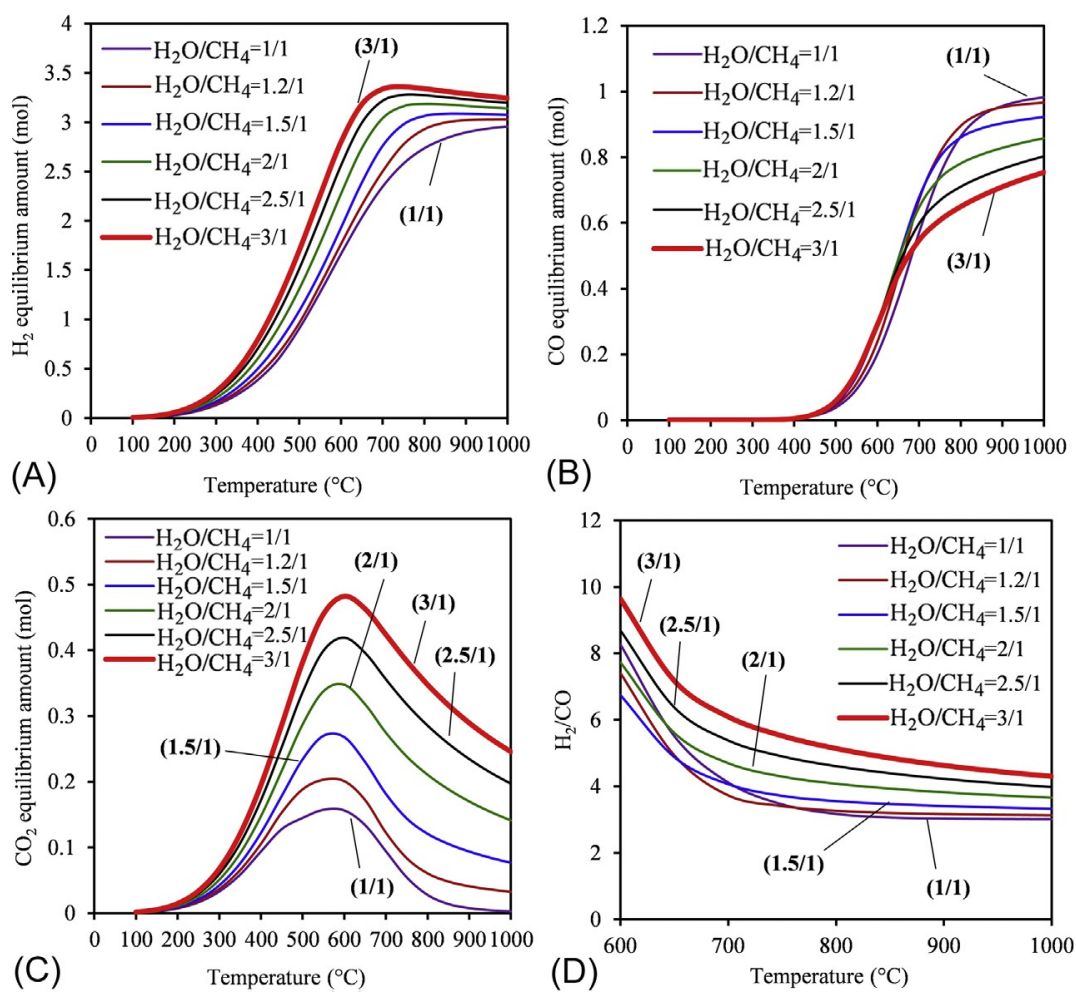
For the molar ratio of H<sub>2</sub>O/CH<sub>4</sub> equal to 3/1 (Fig. 4.1B), solid carbon is potentially eliminated and methane can be completely consumed above around 720°C. This is the main advantage of using a large molar ratio of H<sub>2</sub>O/CH<sub>4</sub>. However, a large excess of water (>50%) strongly burdens the energy balance of the process. Also, carbon dioxide is omnipresent above 200°C because of the WGS reaction (Eq. 4.3 in Table 4.2).

Fig. 4.2 shows CH<sub>4</sub> conversion and coke selectivity as a function of the molar ratio of H<sub>2</sub>O/CH<sub>4</sub> (or S/C) and reaction temperature. Increasing the molar ratio of H<sub>2</sub>O/CH<sub>4</sub> leads to the increase of the CH<sub>4</sub> conversion at a given reaction temperature, and to the decrease of the reaction temperature at a given CH<sub>4</sub> conversion (Fig. 4.2A). Solid carbon can be formed at a low molar ratio of H<sub>2</sub>O/CH<sub>4</sub> of 1/1 and 1.2/1 and can be avoided above 1.5/1 (Fig. 4.2B).

In Fig. 4.3A, as previously observed for CH<sub>4</sub> conversion, at a given reaction temperature, the amount of hydrogen increases with the molar ratio of H<sub>2</sub>O/CH<sub>4</sub>. At a high molar ratio of H<sub>2</sub>O/CH<sub>4</sub> (2/1 to 3/1), the amount of hydrogen reaches a maximum due to the presence of WGS. On Fig. 4.3B, CO can be obtained above 400°C, and its amount increases with the reaction temperature. The molar ratio of H<sub>2</sub>O/CH<sub>4</sub> slightly influences the CO amount up to around 600°C. Then, above this temperature, WGS is favored by increasing the molar ratio of H<sub>2</sub>O/CH<sub>4</sub>, and thus the amount of CO decreases. WGS explains also the



**FIG. 4.2** Influence of the molar ratio of H<sub>2</sub>O/CH<sub>4</sub> and the temperature on (A) CH<sub>4</sub> conversion and (B) coke selectivity at the thermodynamic equilibrium; Initial mixture: 1 mol of CH<sub>4</sub> and 1 to 3 mol of H<sub>2</sub>O.



**FIG. 4.3** Influence of the molar ratio of H<sub>2</sub>O/CH<sub>4</sub> and the temperature on (A) H<sub>2</sub> amount, (B) CO amount, (C) CO<sub>2</sub> amount, and (D) molar ratio of H<sub>2</sub>/CO at the thermodynamic equilibrium; Initial mixture: 1 mol of CH<sub>4</sub> and 1 to 3 mol of H<sub>2</sub>O.

evolution of the amount of  $\text{CO}_2$  in Fig. 4.3C. At a given reaction temperature, the amount of  $\text{CO}_2$  increases with an increase in the molar ratio of  $\text{H}_2\text{O}/\text{CH}_4$ . Also, for each molar ratio of  $\text{H}_2\text{O}/\text{CH}_4$ , the amount of  $\text{CO}_2$  reaches a maximum around  $600^\circ\text{C}$ . The molar ratio of  $\text{H}_2/\text{CO}$  is always higher than 3 and is favorable for all downstream uses as listed in Scheme 4.1, with an eventual regulation of this ratio by WGS.

From these results, it appears that, at atmospheric pressure, SMR is highly favored above  $700^\circ\text{C}$  using a molar ratio of  $\text{H}_2\text{O}/\text{CH}_4 \geq 1.5/1$ .

SMR is not favored at high pressure. However, for different reasons, it can be carried out at 30 bar pressure or even higher in large units. Fig. 4.4 shows the influence of the pressure on the amounts of the main species in SMR at 700, 800, and  $900^\circ\text{C}$  using a mixture of 1 mol  $\text{CH}_4$  and 3 mol  $\text{H}_2\text{O}$ . Under these conditions, the behavior of the system seems to be similar from each other. As expected, increasing the pressure of the reaction strongly burdens the transformation of methane. At each reaction temperature, the amount of  $\text{CH}_4$  increases with an increase of the reaction pressure, which is evidenced in Fig. 4.4D. This leads to a strong decrease in the amount of hydrogen with an increase of the

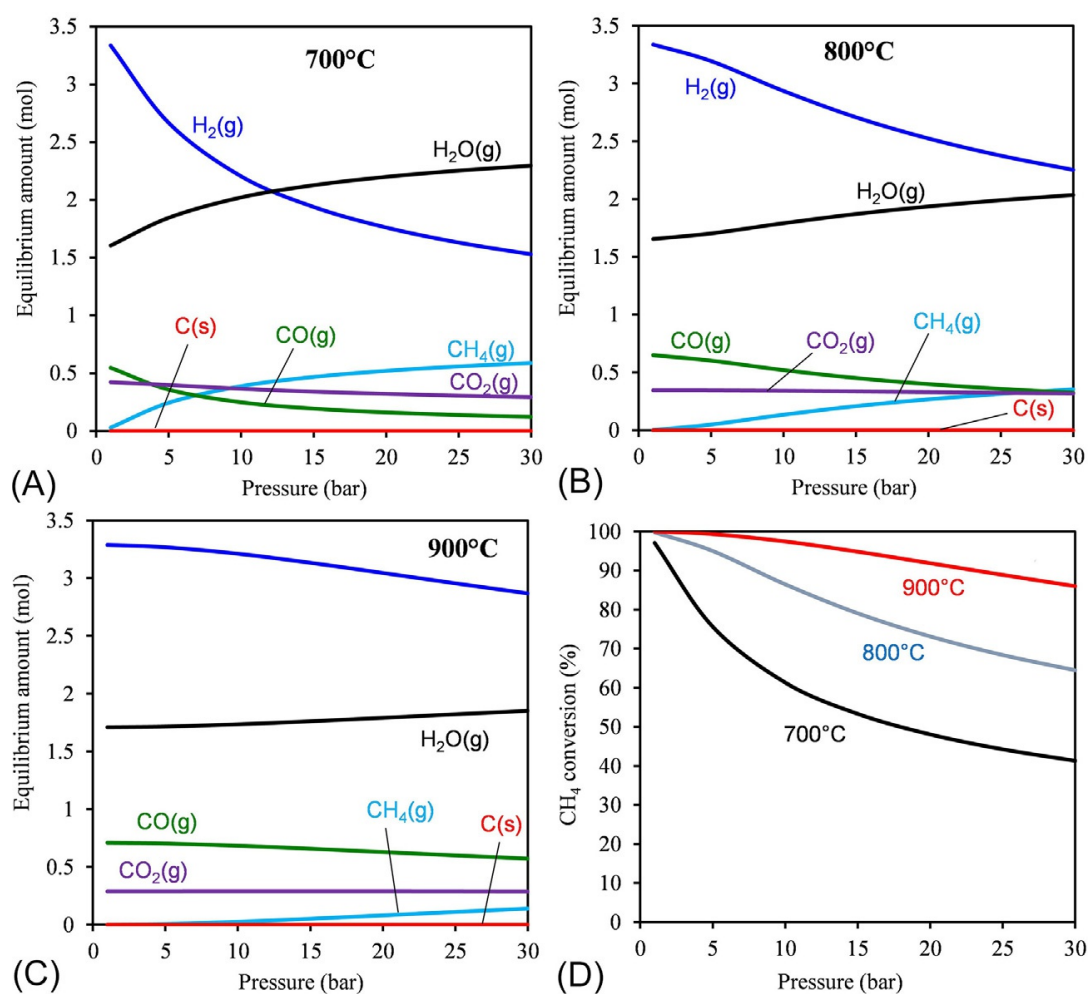


**FIG. 4.4** Influence of the reaction pressure in steam methane reforming in the temperature range of 700– $900^\circ\text{C}$  for a mixture containing 1 mol of  $\text{CH}_4$  and 3 mol of  $\text{H}_2\text{O}$ : (A)  $700^\circ\text{C}$ , (B)  $800^\circ\text{C}$ , (C)  $900^\circ\text{C}$ , and (D)  $\text{CH}_4$  conversion at different temperatures.

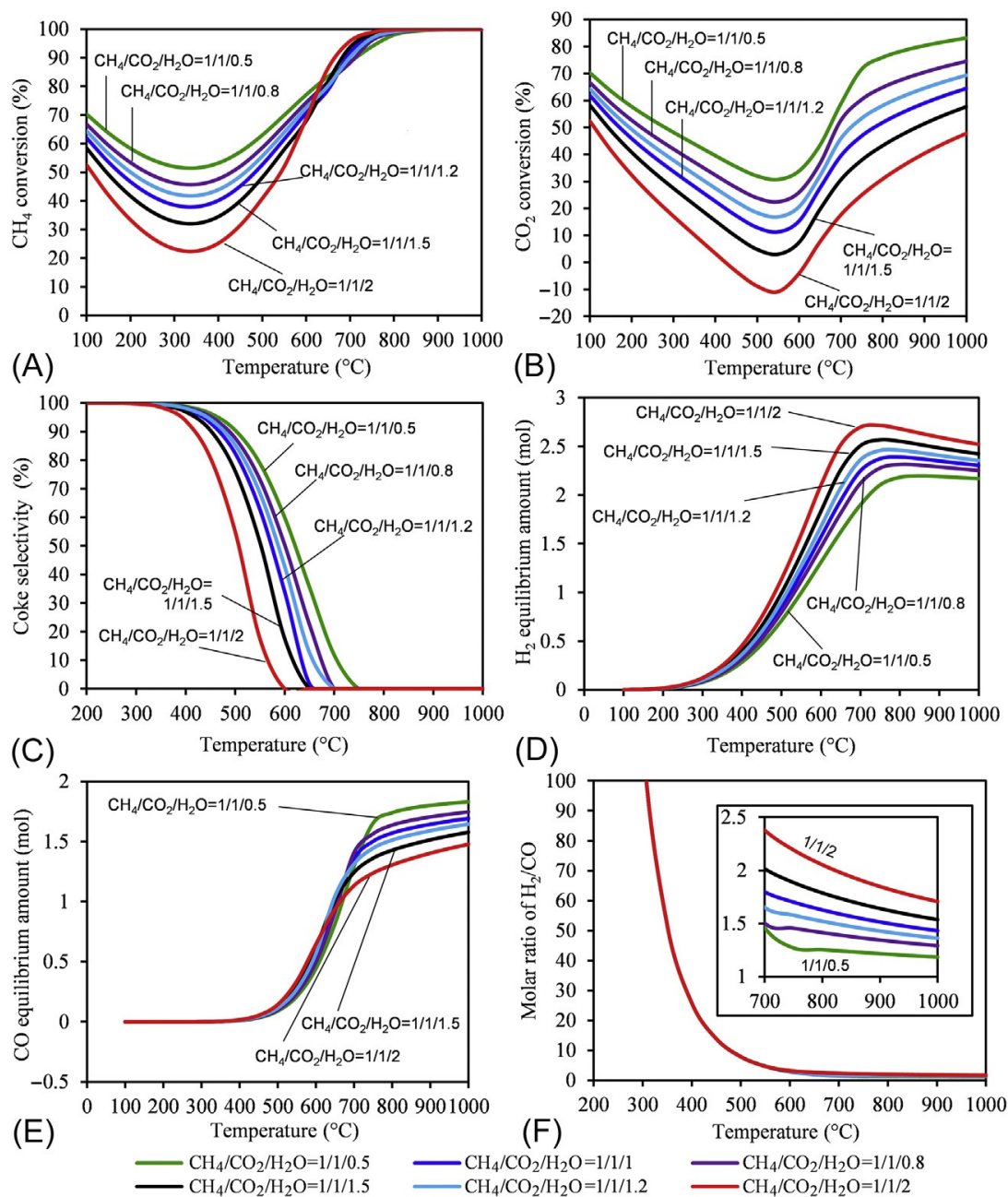
reaction pressure. Increasing the reaction temperature to 900°C does not allow the complete transformation of CH<sub>4</sub> above 5 bar (Fig. 4.4D). No solid carbon is observed under these reaction conditions, as explained previously by a large excess of steam. Because of the WGS, CO<sub>2</sub> is omnipresent in large quantities in the temperature range of 700–900°C.

#### 4.2.2 Thermodynamic Equilibrium of Dual Methane Reforming (Dual-MR)

Dual methane reforming (DMR) refers to the transformation of a CH<sub>4</sub>-CO<sub>2</sub>-H<sub>2</sub>O mixture into syngas. This system is particularly interesting for different configurations, such as steam reforming of biogas and also carbon dioxide valorization by its incorporation into the reforming of methane or natural gas. Thus, both CO<sub>2</sub> and H<sub>2</sub>O play the role of oxidants. The simultaneous presence of CO<sub>2</sub> and H<sub>2</sub>O influences also the WGS equilibrium. Hereafter, we consider two cases: (1) an initial mixture of CH<sub>4</sub> and CO<sub>2</sub> is kept constant, then H<sub>2</sub>O is added in various amounts; and (2) an initial mixture of CH<sub>4</sub> and H<sub>2</sub>O is kept constant, then CO<sub>2</sub> is added in various amounts.

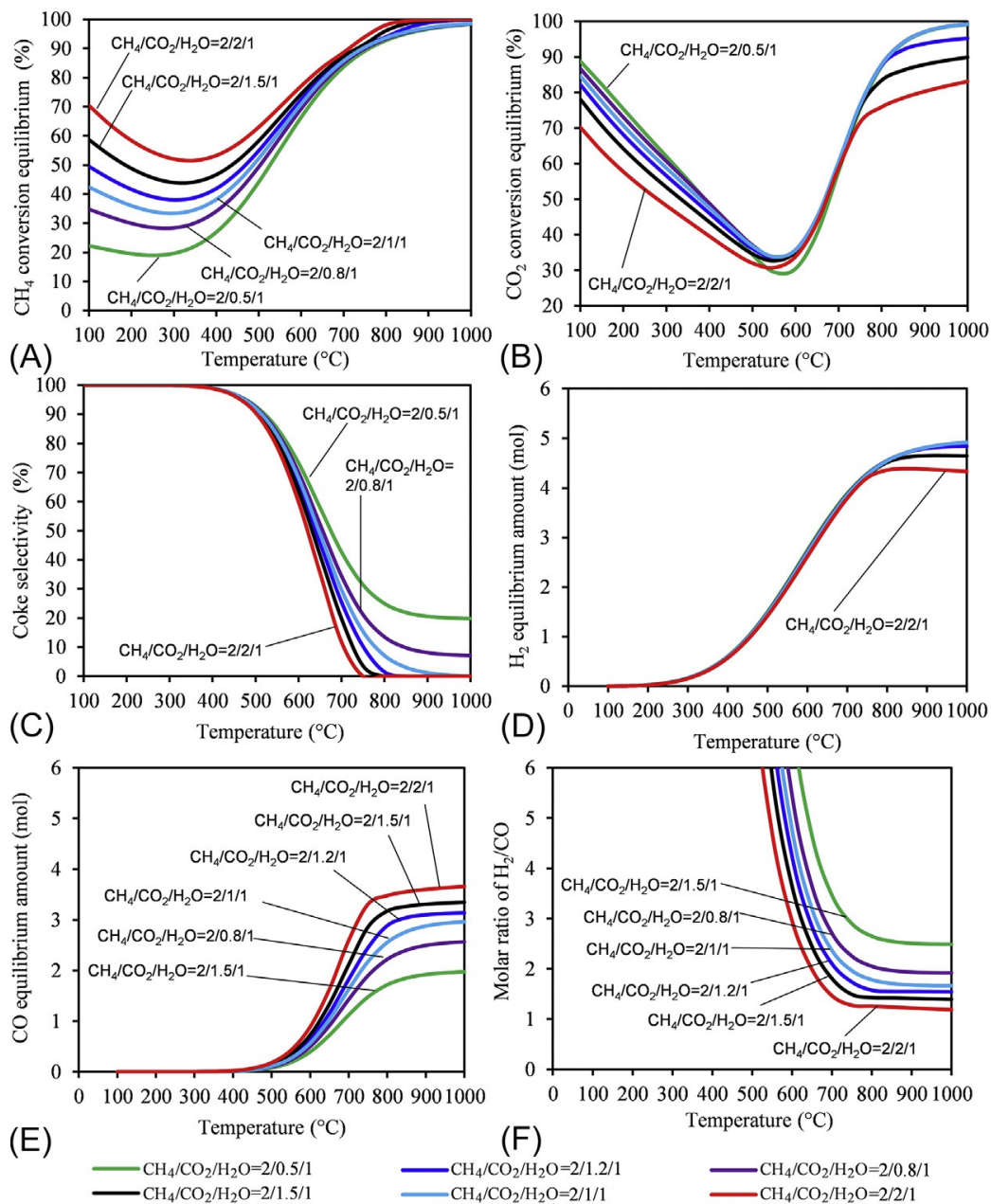
Fig. 4.5 shows the thermodynamic equilibrium of mixtures containing 1 mol of CH<sub>4</sub>, 1 mol of CO<sub>2</sub> and 0.5 to 2.0 mol of H<sub>2</sub>O at 1 bar. The equimolar mixture of CH<sub>4</sub> and CO<sub>2</sub> can represent the composition of a purified landfill gas. Adding water to this mixture is not beneficial for methane conversion under 700°C. In fact, as shown in Fig. 4.5A, the addition of water decreases the methane conversion below 600°C because of the formation of water from the CO<sub>2</sub> and CH<sub>4</sub> mixture by the WGS reaction. Then, above 700°C, the increase in the amount of water leads to a slight increase in CH<sub>4</sub> conversion. Thus, it is possible to reach 100% CH<sub>4</sub> conversion. Also, CO<sub>2</sub> conversion decreases with an increase in the amount of water added to the system. This may be explained by the WGS. On the other hand, the amount of water added to the system strongly influences the amounts of solid carbon, hydrogen, and CO. In Fig. 4.5C, the coke selectivity curve is displaced on the left-hand side, which signifies that coke can be efficiently limited by the addition of water. For hydrogen formation, the addition of water is favorable because of the gasification of the coke. The CO amounts are different from each other above 700°C, as explained by the equilibrium of the WGS. Finally, the molar ratio of H<sub>2</sub>/CO is only slightly affected by the amount of water above 700°C, as highlighted by the insert in Fig. 4.5F.

Fig. 4.6 shows the thermodynamic equilibrium of mixtures containing 2 mol of CH<sub>4</sub>, 1 mol of H<sub>2</sub>O, and 0.5 to 2.0 mol of CO<sub>2</sub> at 1 bar. In this case, the initial amounts of CH<sub>4</sub> and H<sub>2</sub>O are fixed while the amount of CO<sub>2</sub> varies. In Fig. 4.6A, increasing CO<sub>2</sub> helps to notably increase the CH<sub>4</sub> conversion below about 700°C, but this is much less important above this temperature. In Fig. 4.6B and D, the initial amount of CO<sub>2</sub> slightly influences the CO<sub>2</sub> conversion and the amount of H<sub>2</sub>. However, the initial amount of CO<sub>2</sub> has a strong impact on the formation of coke (Fig. 4.6C) and CO (Fig. 4.6E) and the molar ratio of



**FIG. 4.5** Thermodynamic equilibrium of mixtures containing 1 mol of  $\text{CH}_4$ , 1 mol of  $\text{CO}_2$ , and 0.5 to 2.0 mol of  $\text{H}_2\text{O}$  at 1 bar: (A)  $\text{CH}_4$  conversion, (B)  $\text{CO}_2$  conversion, (C) coke selectivity, (D)  $\text{H}_2$  amount, (E)  $\text{CO}$  amount, (F) molar ratio of  $\text{H}_2/\text{CO}$ .

$\text{H}_2/\text{CO}$  (Fig. 4.6F). Above  $500^\circ\text{C}$ , coke selectivity is highly limited by an increasing amount of  $\text{CO}_2$ , and this is explained by the gasification of coke by  $\text{CO}_2$  to form  $\text{CO}$ . This helps to explain also the positive effect of the initial amount of  $\text{CO}_2$  on  $\text{CO}$  formation (Fig. 4.6E). Finally, the  $\text{H}_2/\text{CO}$  molar ratio decreases with the increase of the initial amount of  $\text{CO}_2$  (Fig. 4.6F), explained by the fact that  $\text{H}_2$  formation is less influenced, while  $\text{CO}$  formation is strongly affected, by the initial amount of  $\text{CO}_2$ .



**FIG. 4.6** Thermodynamic equilibrium of mixtures containing 2 mol of  $\text{CH}_4$ , 1 mol of  $\text{H}_2\text{O}$ , and 0.5 to 2.0 mol of  $\text{CO}_2$  at 1 bar: (A)  $\text{CH}_4$  conversion, (B)  $\text{CO}_2$  conversion, (C) coke selectivity, (D)  $\text{H}_2$  amount, (E) CO amount, (F) molar ratio of  $\text{H}_2/\text{CO}$ .

### 4.2.3 Steam Methane Reforming: The SMR Process

As previously mentioned, hydrogen is mostly produced from fossil resources, including natural gas. Using natural gas as feedstock, the hydrogen production process is composed of the following steps:

- Natural gas pretreatment: removal of  $\text{H}_2\text{S}$  and sulfur-containing compounds using a zinc oxide bed, which has high affinity for these pollutants.
- Generation of steam: production of steam from demineralization water. Natural gas can be used as fuel, together with waste heat recovered from the reforming reactor and waste combustible gases from  $\text{H}_2$  separation.

- Steam reforming (Eq. 4.5 in [Table 4.2](#)): reaction of  $\text{CH}_4$  with  $\text{H}_2\text{O}$  to give principally  $\text{CO}$  and  $\text{H}_2$ . Other byproducts are also formed, such as  $\text{CO}_2$  and solid carbon. This is a catalytic process that generally needs a heterogeneous catalyst. As shown in [Table 4.2](#), this reaction is highly endothermic ( $\Delta_r H_{298}^\circ = +206 \text{ kJ/mol}$ ). The thermodynamic study in [Section 4.2.1](#) shows that the reaction is favorable at high temperature (typically  $500\text{--}900^\circ\text{C}$ ) and high steam-to-carbon (S/C) ratio (typically 2.5–3). According to [Fig. 4.2A](#), a high temperature is needed to get high  $\text{CH}_4$  conversion and high chemical kinetic, while a high S/C ratio allows limiting the catalyst deactivation by coke deposition. The reactor for the SMR process is composed of several vertical tubes filled with solid catalysts. These tubes are placed inside a furnace that is heated (using a gas burner for example) to the desired temperature for the SMR reaction ([Linde, n.d.](#)).
- WGS: Syngas from the SMR reactor is cooled down to around  $300\text{--}500^\circ\text{C}$  and then fed into the WGS reactors. Waste heat from this step is recovered and used for steam production. A WGS reactor is classified as either a high-temperature shift reactor (HTSR) or a low-temperature shift reactor (LTSR). Because of the exothermicity of the WGS (Eq. 4.3 in [Table 4.2](#)), a LTSR allows a high  $\text{CO}$  conversion to be obtained. However, its kinetic is slow. On the other hand, a HTSR allows reaching high kinetic, but low  $\text{CO}$  conversion. In general, the combination of both a HTSR and a LTSR leads to higher performance than using only one shift reactor ([Chen et al., 2008](#)).
- $\text{H}_2$  separation: Hydrogen of high purity can be separated from a  $\text{H}_2/\text{CO}_2$  mixture left from a WGS reactor by using the PSA technique (Pressure Swing Adsorption). This technique involves the difference in adsorption capacity of  $\text{H}_2$  compared to other molecules, as well as the fact that adsorption and desorption can be controlled by the increase or decrease of the process pressure.

Concerning the energy balance of hydrogen production from natural gas at an industrial scale, [Table 4.3](#) shows the typical performance figures for a steam reforming–based hydrogen plant of  $50,000 \text{ Nm}^3/\text{h}$ , according to Linde—a world leader in the hydrogen production field ([Linde, n.d.](#)). A fuel consumption of  $744.4 \text{ GJ/h}$  for a production  $50 \text{ kNm}^3/\text{h}$  represents a specific consumption of  $14.88 \text{ MJ/Nm}^3 \text{ H}_2$  and as  $1 \text{ Nm}^3 \text{ H}_2$  contains  $10.82 \text{ MJ/Nm}^3$ , the hydrogen production efficiency is 72.7%; but  $31 \text{ t/h}$  extra steam are exported, so it is a specific steam production of  $0.62 \text{ kg/Nm}^3 \text{ H}_2$  with a heat content of  $3.2 \text{ MJ/kg}$  at  $390^\circ\text{C}$  and an extra  $2.03 \text{ MJ/Nm}^3 \text{ H}_2$ , leading finally to an overall efficiency of 86.2%, including the steam credit. For comparison, hydrogen plants by Air Liquide Engineering & Construction have an energy consumption of  $12.3$  to  $13.2 \text{ MJ/Nm}^3 \text{ H}_2$ , which is comparable to Linde plants ([Air Liquide, n.d.](#)).

The utilization of a reforming catalyst is mandatory for the transformation of methane and oxidants to syngas. Nickel-based catalysts appear as the best choice for both SMR and Dual-MR processes, taking into account their catalytic

**TABLE 4.3** Typical Performance Figures of a Steam Reforming-Based Hydrogen Plant Using Natural Gas as Feedstock

Product hydrogen	Flow Rate	Nm <sup>3</sup> /h	50,000
	Pressure	bar	25
	Purity	mol.%	99.9
Export steam	Flow rate	T/h	31
	Steam temperature	°C	390
	Steam pressure	bar	40
Feed and fuel consumption		GJ/h	744.4
Energy consumption (including steam credit)		GJ/ 1000Nm <sup>3</sup> H <sub>2</sub>	12.853
Utilities	Demineralized water	T/h	55.6
	Cooling water	T/h	160
	Electrical energy	kW	850
Design flexibility	Export steam production	T/ 1000Nm <sup>3</sup> H <sub>2</sub>	0.5–1.2
	Fuel consumption	GJ/ 1000Nm <sup>3</sup> H <sub>2</sub>	0.9–3.5

Adapted from Linde, n.d. [http://www.linde-engineering.in/en/process\\_plants/hydrogen\\_and\\_synthesis\\_gas\\_plants/gas\\_products/hydrogen/index.html](http://www.linde-engineering.in/en/process_plants/hydrogen_and_synthesis_gas_plants/gas_products/hydrogen/index.html) (Accessed on December 13, 2017).

performance and their low cost compared to noble metals, such as Ru, Pt, and Rh (LeValley et al., 2014; Baysal et al., 2017; Ferreira-Aparicio and Benito, 2005). Alumina is also the most appropriate support for these processes (Baysal et al., 2017; Ferreira-Aparicio and Benito, 2005). Alumina-supported nickel catalysts are generally well shaped for use under industrial conditions. The recent review on catalysts for the SMR process by Angeli et al., 2014 confirmed this observation again. The lifetime of a given alumina-supported nickel catalyst is required to be about 5 years under continuous operation (Liu et al., 2010). SMR catalysts can be supplied by different companies, such as Johnson Matthey, BASF, Haldo Topsoe, Thermo Fisher GMBH, and Süd-Chemie (Ferreira-Aparicio and Benito, 2005; Liu et al., 2010).

There are several producers of hydrogen via the SMR process at a large industrial scale: Linde, Haldo Topsoe, Howe-Baker, Foster Wheeler, Sanyo Electric, Osaka Gas Co, Air Liquide, Thyssenkrupp, and others (Linde, n.d.; Ferreira-Aparicio and Benito, 2005; Liu et al., 2010; Shah, 2017). As an example, Linde has built more than 200 plants for hydrogen production with capacities from 1000 to over 100,000 Nm<sup>3</sup>/h (Linde, n.d.). Air Liquide Engineering & Construction provides solutions for hydrogen plants with capacities in the range of 10,000–200,000 Nm<sup>3</sup>/h of hydrogen (Air Liquide, n.d.).

#### 4.2.4 Steam Biogas Reforming: The SBR Process

Most of the features of the SMR process presented in the previous section are still valid for the steam biogas reforming (SBR) process. One of the most important differences is the capacity of the units: biogas production plants have a capacity ranging from 100 Nm<sup>3</sup>/h for small agricultural or agro-food waste digesters to a few 1000 Nm<sup>3</sup>/h for large municipal waste landfills; moreover, in some cases all of the biogas is not converted to hydrogen and other biogas valorization can coexist on the site. Thus, biogas steam reforming processes have to be designed for capacities ranging from 50 to 1000 Nm<sup>3</sup> H<sub>2</sub>/h. The example presented in this section is relative to a 50 Nm<sup>3</sup> H<sub>2</sub>/h production unit to be realized in 2018 by ALBHYON HERA's office under the VABHYOGAZ project on the site of TRIFYL's bioreactor, which produces about 1500 Nm<sup>3</sup>/h of biogas, 40 km from the city of Albi (Occitanie region, France). This unit has a capacity about 1000 times smaller than the industrial SMR process presented in the previous section. Yet it produces more than 100 kg H<sub>2</sub>/day, enough to travel 10,000 km/day on hydrogen. It is adapted to supply several tens of cars per day, refueling each with a few kg H<sub>2</sub>, and this is the size of fuel cell car fleets for the next few years. As biogas sources are located in many places all over the territory, this underlines an important feature of biogas steam reforming: it concerns distributed hydrogen production.

A second difference with respect to large SMR processes is the integration of the SBR process on the site, which is radically different in that there is no need for steam on biogas production sites: in most cases, SBR has to be a standalone process and so efficiency optimization is more difficult. When another biogas valorization process coexists on the biogas production site, some interaction between the two processes can be implemented in order to improve efficiency or simplify the process and lower the investment cost; an example is shown here.

Then, of course, an important difference comes from the nature of the feedstock in that biogas contains more CO<sub>2</sub> than natural gas. The typical composition of the biogas feeding the SBR process at the TRIFYL bioreactor is given in Table 4.4.

Until now, the choice of designers for biogas reforming has been mainly to add a preliminary step in the process in order to extract the CO<sub>2</sub> from the

**TABLE 4.4** Composition of the Biogas Feeding the Steam Biogas Reforming Process

Biogas Composition	Molar Fraction	Mass Fraction
CH <sub>4</sub>	59.75%	35.05%
CO <sub>2</sub>	40.0%	64.60%
N <sub>2</sub>	0.20%	0.20%
O <sub>2</sub>	0.04%	0.05%
H <sub>2</sub> S	725 ppmv	900 ppm

mixture and then to reform the methane in a classical SMR. This preliminary step for CO<sub>2</sub> separation, also called enrichment of the biogas, can be done through PSA, or amines absorption, or membrane permeation. This case in which SBR is Enrichment + SMR has the disadvantage of increasing the complexity and the investment cost of the overall process. “Direct SBR” is considered here, without preliminary enrichment and with steam injected into the reforming reactor. Thus, it is a form of DMR, and is, in fact, not new as a commercial process for DMR, in that SPARG was developed 30 years ago by Haldor-Topsoe (Rostrup-Nielsen, 2002). Here the feeding ratio CH<sub>4</sub>/CO<sub>2</sub> is 1/0.67, in the range explored in Section 4.2.2. Yet, for a given CH<sub>4</sub> flow rate feeding the process, the total volume flow rate is increased by a factor of 1.67 and the total mass flow rate is increased by a factor of 2.85 due to the presence of CO<sub>2</sub>. Thus, the aerodynamic, thermal, and chemical behaviors of the mixture are considerably modified in the equipment used for the SBR process as compared to the SMR process. The process developed under the VABHYOGAZ project has been designed so that, through its control system, it can deal with these different behaviors and manage mixtures with CH<sub>4</sub>/CO<sub>2</sub> ratios ranging from 1/0 to 1/1. The nature of the CO<sub>2</sub> must be emphasized: SMR, when applied to natural gas, produces large amounts of CO<sub>2</sub> with a fossil origin. On the other hand, SBR also produces CO<sub>2</sub>, but this CO<sub>2</sub> comes from the biodegradation of green waste or of agro-food waste; it has no fossil origin as it was previously captured by plants from the atmosphere. Thus, the SBR process does not add any fossil CO<sub>2</sub> or greenhouse gas to the atmosphere and produces renewable hydrogen.

The successive steps of the SBR process are similar to those of the SMR process, with the necessary adaptations to accommodate the different features, as explained above. These steps are sketched in Fig. 4.7 and presented here, together the main operating parameters:

- Biogas cleaning: H<sub>2</sub>S and other sulfur compounds are removed by adsorption on an active carbon-fixed bed.
- Compression of the biogas: the PSA requires pressure to be efficient and it costs less energy to compress the biogas and liquid water before reforming

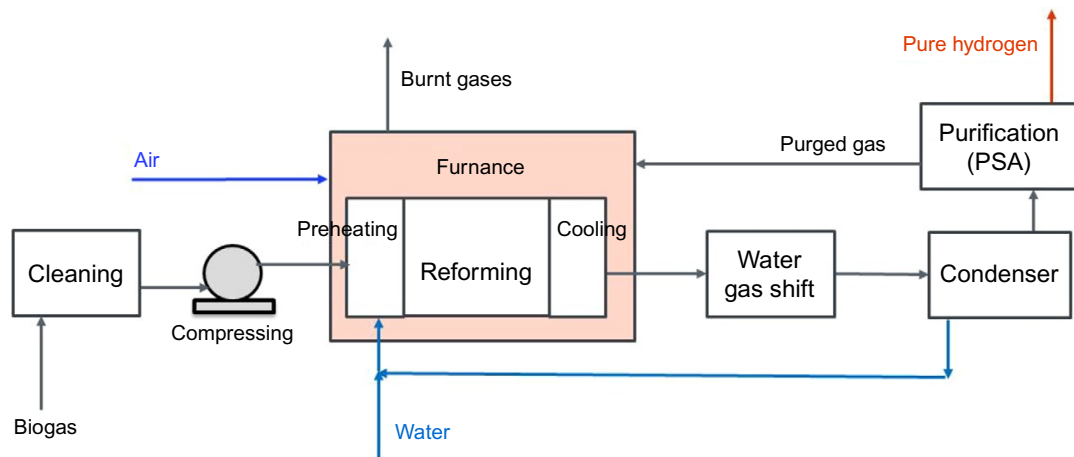


FIG. 4.7 Block diagram of the SBR process in the VABHYOGAZ project.

than compressing the gas mixture after reforming. The pressure level here is 15 bar. As seen in the previous section, increasing the pressure has a negative effect on  $\text{CH}_4$  conversion, but at this level, the residual  $\text{CH}_4$  is low.

- Heating of biogas, vaporization and overheating of water: this is mainly realized in a specific zone inside the reforming tubes through heat recovery from the reformat gas before it leaves the tubes and through exchange with the combustion gases.
- SBR (Eq. 4.5) on a catalytic fixed bed inside the reforming tubes. The heat for this highly endothermic reaction ( $\Delta_r H_{298}^\circ = +206 \text{ kJ/mol}$ ) is provided through exchange with the combustion gases inside the furnace where the tubes are placed. The reaction temperature is  $860^\circ\text{C}$  and the S/C ratio is 3; for a production of  $50 \text{ Nm}^3 \text{ H}_2/\text{h}$ , the reformed biogas flow rate is  $31.7 \text{ Nm}^3/\text{h}$  and the water flow rate is  $45.6 \text{ kg/h}$ . With these operating parameters, a chemical equilibrium calculation shows no carbon formation and a 100%  $\text{CH}_4$  conversion. Nevertheless, as indicated in Table 4.5, some residual  $\text{CH}_4$  is assumed, corresponding to an imperfect catalytic effect.
- Cooling of the reformat gas mixture down to  $300^\circ\text{C}$  before leaving the tubes.
- WGS catalytic reactor to convert CO and water into  $\text{H}_2$  and  $\text{CO}_2$  (Eq. 4.3). The heat from this exothermic reaction ( $\Delta_r H_{298}^\circ = -41 \text{ kJ/mol}$ ) is valorized for preheating and partial vaporization of water. WGS is conducted in 2 steps: first, HTSR around  $300^\circ\text{C}$ , and then LTSR around  $200^\circ\text{C}$ . The CO level is decreased to 1.5%.
- Cooling the reformat mixture down to  $10^\circ\text{C}$  through exchange with cold water. Most of the water contained in the reformat mixture condenses and can be recycled as reforming water.
- $\text{H}_2$  separation using a PSA. The purity achieved for hydrogen is 99.995%. At 15 bar, the PSA efficiency is 79%, which means that 21% of the produced hydrogen leaves the PSA with the purged gases, which also contain  $\text{CO}_2$  and residual CO and  $\text{CH}_4$ .
- The pure hydrogen can then be compressed and stored at high pressure.

**TABLE 4.5 Gas Composition in the 50 Nm<sup>3</sup> H<sub>2</sub>/h SBR Process**

Volume Fractions	Reformed Biogas	Reforming Water	Reformer Output	WGS Output	Condenser Output	PSA Output	PSA Purged Gas	Burnt Gases
H <sub>2</sub>	0		40.2%	52.3%	66.6%	>99.9995%	29.5%	
H <sub>2</sub> O	0	100%	33.6%	21.5%	0.1%		0.2%	16%
N <sub>2</sub>	0,2%		0.1%	0.1%	0.1%		0.1%	56.5%
CO	0		13.6%	1.5%	1.9%	<1 ppm	4.0%	
CO <sub>2</sub>	40%		10.3%	22.5%	28.6%		60.3%	24.5%
CH <sub>4</sub>	59.7%		2.2%	2.2%	2.8%		5.9%	
Other	O <sub>2</sub> , H <sub>2</sub> S							O <sub>2</sub> 3%
Flow rate (kg/h)	38.5	45.6	84.1	84.1	63.3	4.47	58.3	195.8

- Heat production in the furnace surrounding the reforming tubes comes from the combustion of the purged gases. The energy needed is 72.3 kW to balance the SMR endothermicity and to complete the vaporizing and overheating of water and biogas. The energy available in the purged gases is 74 kW and taking into account the energy losses in the exhaust gases, a complement must be provided by some biogas injected into the furnace; 3.7 Nm<sup>3</sup>/h of biogas are added to supply 22 kW. It can be noticed here that as long as the energy contained in the purged gas is lower than the energy to be burnt in the furnace, there is no need to improve the PSA efficiency, nor the CH<sub>4</sub> conversion in the reforming tube, nor the CO conversion in the WGS reactor as any decrease in the H<sub>2</sub>, CH<sub>4</sub> or CO content of the purged gas should be balanced by an extra injection of biogas in the furnace.

A better way to valorize the purged gases may be considered when another valorization process coexists on site (electricity production in gas engines for example), especially when the flow of reformed biogas is small with respect to the total available biogas flow, as in the present case. Then, the purged gases can be returned and mixed with the flow of biogas feeding the other process for electricity production. Heat production in the furnace is then realized with biogas only: 14 Nm<sup>3</sup>/h of biogas supply 84 kW to the furnace. With this integration, thanks to the interaction between the two processes, the global efficiency, including the purged gas credit, is increased from 71% to 82%, as presented in [Table 4.6](#).

It must be pointed out that the SBR process, similar to SMR process, is an energy-intensive process, and high-temperature thermal integration is the key to reach good efficiency. For a 150 kW hydrogen output, the reforming reaction heat (206 kJ/mol CH<sub>4</sub>) is 48.3 kW (32.2% of the hydrogen energy content) and this heat

**TABLE 4.6** Energy Efficiency of a 50 Nm<sup>3</sup>H<sub>2</sub>/h SBR Process With Two Options, a Standalone Process or an Integrated Process With Purged Gas Credit

Parameter	Stand-Alone Process	Integrated Process
Reformed biogas flow rate (Nm <sup>3</sup> /h)	31.7	31.7
Combustion biogas flow rate (Nm <sup>3</sup> /h)	3.7	14
Purged gas energy returned to the main biogas flow (kW)	0	74
Energy in the produced hydrogen (kW)	150	150
Hydrogen energy efficiency (% LHV)	71.3	55.7
Energy efficiency with purged gas credit (% LHV)	71.3	82.4

**TABLE 4.7** Energy Repartition of the SBR Process With 150 kW Hydrogen Output

Energy needs	Energy sources
Reaction heat: 48.3 kW (32.2%)	Combustion of purges gas and extra biogas 72.3 kW
Preheating of the reactants (water and biogas): 71.3 kW (47.5%)	
Total : 119.6 kW (79.7% of hydrogen energy content)	

has to be brought through an external exchange at very high temperature to reach the 860°C reacting temperature. Together with preheating, vaporizing, and overheating of water and biogas, it is 119.6 kW (79.7% of the hydrogen energy content) to be brought to the reactants, among which 13.8 kW come from the WGS reactors (11.6%), 33.5 kW come from the cooling of the reformat mixture (28%), and the remaining 72.3 kW come from the furnace (60.4%) (Table 4.7).

For this small-capacity unit, the electric consumption of the auxiliaries is estimated to be 12.6 kW and the main parts are for biogas compression (5.7 kW) and for refrigeration (3.6 kW). This can be compared to the 750 kW for the 1000 times larger SMR process, in which natural gas compression is not included, as natural gas is delivered at a sufficient pressure from the pipe. It appears the small-scale effect is sensible: excluding compression, auxiliary consumption is divided by 100 (from 750 to 7.5 kW) when capacity is divided by 1000 (from 50,000 to 50 Nm<sup>3</sup> H<sub>2</sub>/h).

#### 4.2.5 Kinetic of Steam Methane Reforming

Kinetic data on the SMR process are rich after several decades of research and development. Because the process is complex, with numerous intermediate steps, and because of the nature of kinetic parameters, which strongly depend on experimental conditions, it is difficult to achieve a general agreement on kinetic models. Discrepancies, even contradictions, exist as reported in the literature (Liu et al., 2010; Nguyen et al., 2014). The most common kinetic laws considered for the SMR process are: Langmuir-Hinshelwood, Temkin, Eley-Rideal, power law, and microkinetic analysis (Soria et al., 2012; Temkin, 1979). Table 4.8 summarizes some selected models and results reported in the literature.

**TABLE 4.8 Selected Kinetic Models for SMR**

Catalyst	Condition	Kinetic Model and Parameters	Equations	Reference
Ni/MgAl <sub>2</sub> O <sub>4</sub>	773–848 K 3–15 bar	$r_1 = \frac{k_1}{p_{H_2}^{2.5}} \frac{p_{CH_4} p_{H_2O} - \frac{p_{H_2}^3 p_{CO}}{K_1}}{(DEN)^2}$ $DEN = \frac{1 + K_{CO} p_{CO} + K_{H_2} p_{H_2} + K_{CH_4} p_{CH_4} + K_{H_2O} p_{H_2O}}{p_{H_2}}$ <p><math>k_1 = 0.2088, 0.5254</math> and <math>2.069 \text{ kmol bar}^{0.5} \text{ kg}^{-1} \text{ h}^{-1}</math> at 773, 798 and 823 K, respectively  <math>A (k_1) = 4.225E+15</math>  <math>E_1 = 240.1 \text{ kJ/mol}</math></p>	(4.12)	Xu and Froment (1989)
NiO/Al <sub>2</sub> O <sub>3</sub>	573–973 K 1 bar	$R_1 = \frac{k_1}{p_{H_2}^{2.5}} \left( p_{CH_4} p_{H_2O} - \frac{p_{H_2}^3 p_{CO}}{K_1} \right) \left( \frac{1}{\Omega^2} \right)$ $\Omega = 1 + K_{CO} p_{CO} + K_{H_2} p_{H_2} + K_{CH_4} p_{CH_4} + K_{H_2O} \frac{p_{H_2O}}{p_{H_2}}$ <p><math>k_{O,1} = 5.19E+9 \text{ mol bar}^{0.5} \text{ g}^{-1} \text{ s}^{-1}</math>  <math>E_1 = 257.01 \text{ kJ/mol}</math></p>	(4.12)	Abbas et al. (2017)
Ni/YSZ	773–1013 K 1 bar	$r_r, Arr = k \cdot p_{CH_4}^\beta \cdot p_{H_2O}^\beta$ <p><math>k = 40 \pm 1 \text{ s}^{-1}</math> at 773 K and <math>393 \pm 48 \text{ s}^{-1}</math> at 1013 K when S/C=2  <math>E_a = 62 \pm 1 \text{ kJ/mol}</math></p>	(4.13)	Nguyen et al. (2016)
Ru/SiO <sub>2</sub>	723–823 K 1 bar	$r_1 = \frac{k_1}{p_{H_2}^{2.5}} \theta^2 p_{CH_4} p_{H_2O} (1 - \beta_1)$ <p><math>k_1 = 4.6 \text{ mol kg}_{cat}^{-1} \text{ s}^{-1} \text{ Pa}^{0.5}</math> at 773 K; <math>E_a = 140 \text{ kJ/mol}</math></p>	(4.14)	Soria et al. (2012)

Continued

**TABLE 4.8** Selected Kinetic Models for SMR — cont'd

Catalyst	Condition	Kinetic Model and Parameters	Equations	Reference
Ru/Al <sub>2</sub> O <sub>3</sub>	823–1023 K 1–5 bar	$r_f = k \times P_{\text{CH}_4}$ $E_a = 91 \text{ kJ/mol}$	(4.15)	Wei and Iglesia (2004a, b)
Rhodium- and Nickel-based catalysts	723–1023 K 1 bar	$r_f = k \times P_{\text{CH}_4}$ $E_a = 69.1 \text{ kJ/mol}$ and $k_{0a} = 2.88\text{E} + 6 \text{ s}^{-1}$ for Rh catalyst $E_a = 96.1 \text{ kJ/mol}$ and $k_{0a} = 7.26\text{E} + 7 \text{ s}^{-1}$ for Ni catalyst	(4.15)	Zeppieri et al. (2010)

The model proposed by [Xu and Froment \(1989\)](#) is based on Langmuir-Hinshelwood methodology and is usually considered as the most widely used model for the SMR process. In this model, various chemical reactions were considered in order to explain the formation of different products, including H<sub>2</sub>, CO, CO<sub>2</sub>, H<sub>2</sub>O, and solid carbon (C). The following assumptions were made to build reaction schemes of the SMR process ([Xu and Froment, 1989](#)):

- Water reacts with surface nickel atoms, yielding adsorbed oxygen and gaseous hydrogen.
- Methane is adsorbed on surface nickel atoms. The adsorbed methane either reacts with the adsorbed oxygen or is dissociated to form chemisorbed radicals.
- The concentrations of the carbon-containing radicals are much lower than the total concentration of the active sites.
- The adsorbed oxygen and the carbon-containing radicals react to form oxygen-containing radicals.
- The hydrogen formed is directly released into the gas phase and/or the gaseous hydrogen is in equilibrium with adsorbed atomic or molecular hydrogen.
- All reaction schemes have a rate-determining step among the following reactions: SMR, WGS, and the direct formation of CO<sub>2</sub> and H<sub>2</sub> from CH<sub>4</sub> and H<sub>2</sub>O (reactions 4.3, 4.5, 4.11 in [Table 4.2](#)).

After the work reported by [Xu and Froment \(1989\)](#), other research confirmed the validity of this model for the SMR process, such as the recent work of [Abbas et al. \(2017\)](#).

[Nguyen et al. \(2016\)](#) studied the kinetic of the SMR process by expressing the reaction rate as a function of the exponential of methane and steam pressure (power law). They highlighted also that the reaction order (for methane and steam) varies significantly, as reported by several studies. The value of  $\alpha$  (reaction order with respect to partial pressure of methane) was typically found in the range of 0.85–1.4, while the value of  $\beta$  (reaction order with respect to partial pressure of steam) can be negative, zero, or positive depending strongly on the ratio of steam/carbon (S/C). Small S/C ratios yield positive  $\beta$ , S/C ratios on the order of 2 yield  $\beta$  close to zero, and high S/C ratios yield negative  $\beta$ . In their study, [Nguyen et al. \(2016\)](#) found the value of  $\alpha$  and  $\beta$  to be equal to 2 and 1, respectively, for S/C ratios of 2–3, and an activation energy,  $E_a$ , equal to  $62 \pm 1$  kJ/mol.

As previously assumed by [Xu and Froment \(1989\)](#) and other researchers and based on a thermodynamic analysis of the SMR process under the studied conditions, three reactions build the kinetic mechanism of the process, which are the reactions (4.3), (4.5), (4.11) in [Table 4.2](#). Thus, methane is dissociated on nickel sites. In the study of [Soria et al. \(2012\)](#), the SMR process was carried out at 723–823 K and 1 bar over a Ru/SiO<sub>2</sub> catalyst. Their kinetic models were

built by supposing that both methane and steam react as adsorbed species. Thus, steam can be adsorbed on the catalyst surface with or without dissociation, while methane presents more possibilities for dissociation, forming C or the intermediate specie  $\text{CH}_2$ . The combination of these possibilities yields a total of six kinetic mechanisms. Among these, the best kinetic model was found by fitting with the experimental data, and the reaction rate equation is shown in [Table 4.8](#) (Eq. 4.14). For this kinetic model, the following assumptions were made:

- Steam is dissociated into gaseous  $\text{H}_2$  and adsorbed O when it is adsorbed on the catalyst surface.
- Methane is adsorbed to form the intermediate  $\text{CH}_{2(\text{ads})}$ , which later reacts with oxygen to form  $\text{CHO}_{(\text{ads})}$ .
- $\text{CHO}_{(\text{ads})}$  species react in parallel to form CO and  $\text{CO}_2$ . These surface reactions that produce CO and  $\text{CO}_2$  are considered to be the rate controlling steps.
- Also, WGS takes place.
- Desorption of adsorbed CO,  $\text{CO}_2$  species, and a combination of adsorbed H species to form gaseous CO,  $\text{CO}_2$  and  $\text{H}_2$ .

The activation energy was found to be 140 kJ/mol for the SMR reaction over a Ru/SiO<sub>2</sub> catalyst ([Soria et al., 2012](#)).

In their earlier study, [Wei and Iglesia \(2004a, b\)](#) experimentally studied the SMR process using a Ru/Al<sub>2</sub>O<sub>3</sub> catalyst at 823–1023 K and 1–5 bar. They found that the reaction rate depends only on the partial pressure of methane and not on the partial pressure of steam. Thus, the global kinetic equation is simple, as shown in Eq. (4.15) in [Table 4.8](#). They also obtained a similar result for the CO<sub>2</sub> reforming of methane in this study. This kinetic mechanism was later confirmed by [Zeppieri et al. \(2010\)](#), using rhodium- and nickel-based catalysts. Note that in these two papers, both research groups used a very small quantity of catalyst. [Wei and Iglesia \(2004a, b\)](#) used 5 mg of catalyst (250–425 μm) diluted in 500 mg of acid-washed quartz powder (250–425 μm) to fill a quartz or steel tube (8 mm inner diameter). [Zeppieri et al. \(2010\)](#) used 5–30 mg of catalyst samples diluted with 500–1500 mg of acid-washed silicon dioxide to fill a quartz tube reactor of 8 mm inner diameter. The absence of preferential passage of reactants through the catalytic bed should be confirmed, considering the small quantities of catalysts versus the reactor inner diameter of 8 mm.

As a partial conclusion, there have been several kinetic studies of the SMR process. Because the process is complex, with the implication of different chemical equilibriums, different kinetic models have been built and discussed. The validation of a given model is generally done by fitting with the experimental data. Thus, it is only meaningful to retain a kinetic mechanism taking into account the experimental conditions. More effort is still needed to determine the intrinsic kinetic of the SMR process.

## 4.3 DRY REFORMING OF METHANE

### 4.3.1 Thermodynamic Equilibrium Aspect

DRM relates to the reaction between  $\text{CH}_4$  and  $\text{CO}_2$  to form  $\text{CO}$  and  $\text{H}_2$  (Eq. 4.1 in Table 4.2). According to Eq. (4.1), 1 mol of  $\text{CO}_2$  is needed to reform 1 mol of  $\text{CH}_4$ . Fig. 4.8 shows the thermodynamic equilibrium of an equimolar mixture of  $\text{CH}_4$  and  $\text{CO}_2$  at atmospheric pressure. Only the main species are presented. Methane conversion increases above  $350^\circ\text{C}$  and reaches more than 98% at  $900^\circ\text{C}$ . Solid carbon and water are highly selected below  $600^\circ\text{C}$ . Above this temperature,  $\text{CO}$  and  $\text{H}_2$  become the main products. Taking into account the conversion of  $\text{CH}_4$  and  $\text{CO}_2$ , and the selectivity of the reaction, this process should be carried out at  $850^\circ\text{C}$  or above.

Fig. 4.9 shows the influence of the molar ratio of  $\text{CO}_2/\text{CH}_4$  on the thermodynamic equilibrium of a  $\text{CO}_2$  and  $\text{CH}_4$  mixture. Increasing this ratio increases

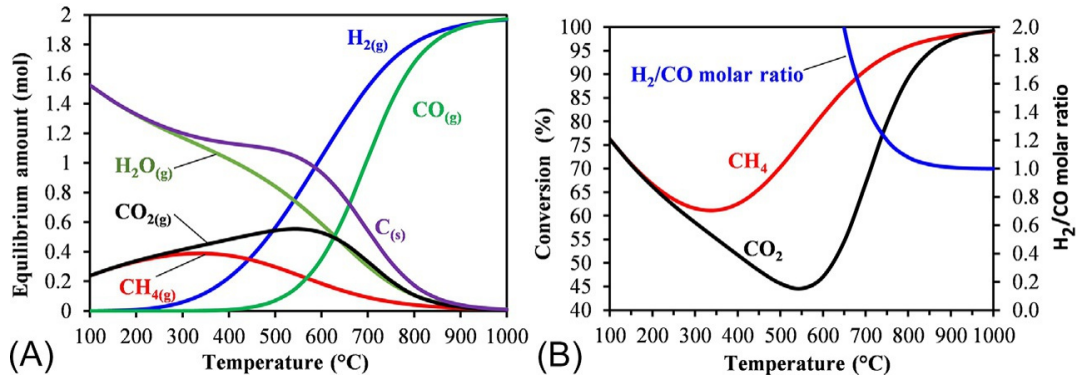


FIG. 4.8 Thermodynamic equilibrium at 1 bar of the equimolar mixture of  $\text{CH}_4$  and  $\text{CO}_2$  (A) and the corresponding  $\text{CH}_4$  and  $\text{CO}_2$  conversion and molar ratio of  $\text{H}_2/\text{CO}$  (B).

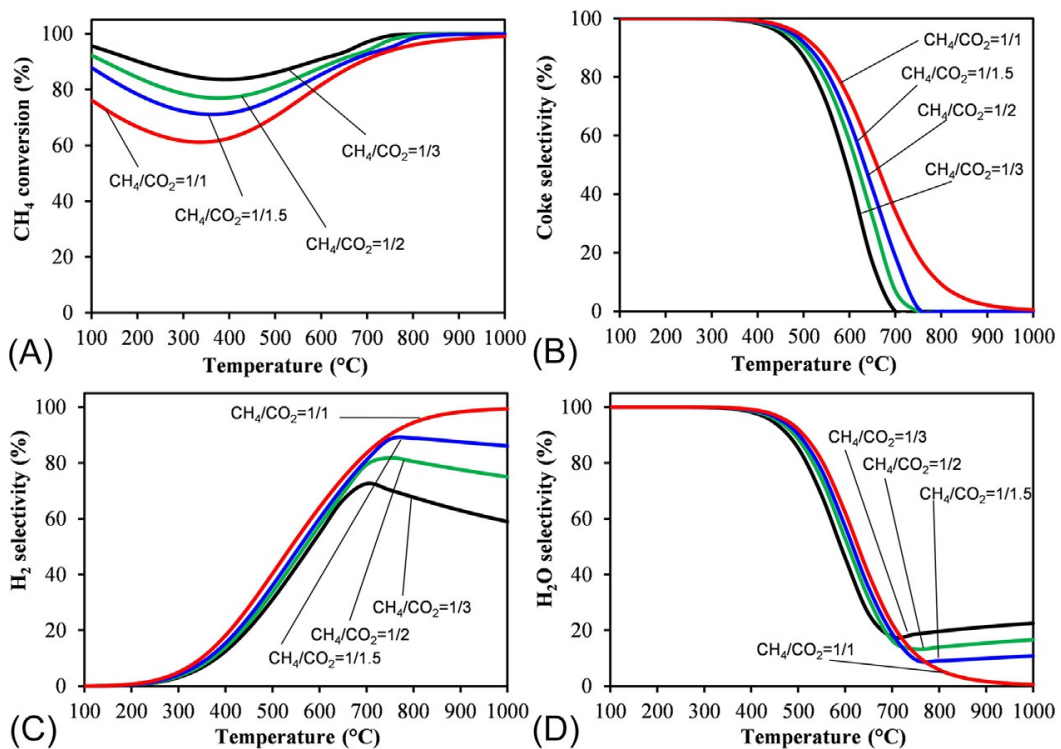
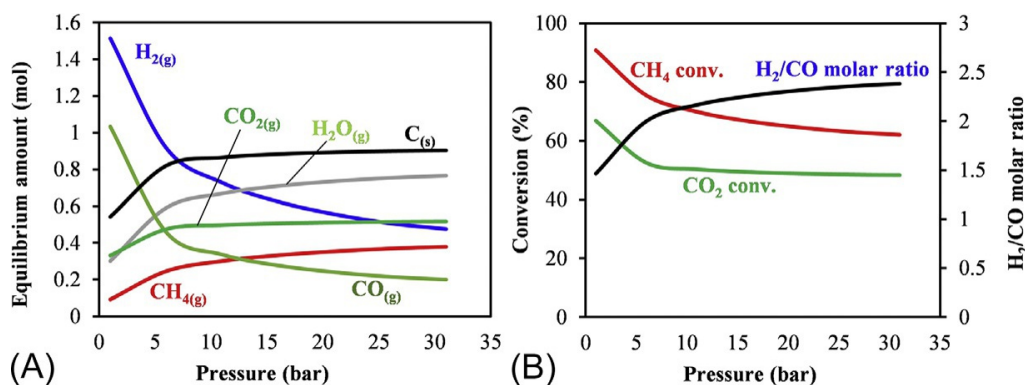


FIG. 4.9 Thermodynamic equilibrium at 1 bar of mixtures containing 1 mol of  $\text{CH}_4$  and 1 to 3 mol of  $\text{CO}_2$ : (A)  $\text{CH}_4$  conversion, (B) coke selectivity, (C)  $\text{H}_2$  selectivity, and (D)  $\text{H}_2\text{O}$  selectivity.



**FIG. 4.10** Influence of the reaction pressure on the equilibrium of an equimolar mixture of CH<sub>4</sub> and CO<sub>2</sub> at 700°C.

methane conversion at a given temperature and decreases coke selectivity. At a ratio of CO<sub>2</sub>/CH<sub>4</sub> equal to 3, coke can be avoided above 700°C. However, adding more CO<sub>2</sub> influences also WGS (Eq. 4.3 in Table 4.2). Consequently, the amount of H<sub>2</sub> decreases and the amount of H<sub>2</sub>O increases. Thus, the choice of CO<sub>2</sub>/CH<sub>4</sub> molar ratio must integrate all the factors, i.e., reaction conversion, reaction selectivity, and energy consumption, in order to optimize the DRM process, in particular for H<sub>2</sub> production.

High pressure is generally not favorable for the DRM process. Fig. 4.10 presents the influence of the reaction pressure on the thermodynamic equilibrium of an equimolar mixture of CH<sub>4</sub> and CO<sub>2</sub> at 700°C. Methane conversion decreases quickly from 91 to 62% when the pressure increases from 1 to 30 bar. In parallel, the amounts of CO and H<sub>2</sub> drastically decrease while the amounts of H<sub>2</sub>O and solid carbon strongly increase with the increase of the reaction pressure. Thus, DRM at high pressure is not recommended.

### 4.3.2 Catalysts for Methane Dry Reforming

Because DRM is an extremely endothermic reaction, one of the main challenges in the heterogeneous catalytic DRM process is the considerable loss of catalytic activity with time-on-stream (TOS) due to the formation of carbonaceous species on the catalyst surface from CH<sub>4</sub> cracking and metal sintering (Argyle and Bartholomew, 2015; Usman et al., 2015). Thus, numerous studies have been conducted to seek for ideal and cost-effective solutions to overcome the limitations in catalytic stability during DRM. In general, the employment of noble metal catalysts (namely, Pt, Ru, and Rh) could solve the above-mentioned problems with high catalytic activity and coke resistance (Jones et al., 2008; Pakhare and Spivey, 2014). However, the high cost and limited availability of noble metals have limited their use in industrial applications. For these reasons, catalyst development has tended to shift toward the design of metal catalysts other than noble metals, such as Ni- and Co-based catalysts, which are globally available and more economical. In order to achieve catalyst activity and stability comparable to those of precious metals, tuning catalytic properties by

modification of supports and addition of promoters has become a main focus area in many studies (Wang et al., 2017; Qian et al., 2014; Zarei et al., 2016; Djinović and Pintar, 2017). The recent efforts in designing promoted and supported nonnoble metal catalysts for DRM are comprehensively discussed in this section.

#### 4.3.2.1 Catalyst Supports

The active metals (including noble metals, Ni, and Co) for DRM are normally dispersed on various single-metal oxides possessing basic ( $\text{CeO}_2$  and  $\text{La}_2\text{O}_3$  according to Barroso-Quiroga and Castro-Luna, 2010), acidic ( $\text{SiO}_2$ , amphoteric  $\gamma\text{-Al}_2\text{O}_3$  (Barroso-Quiroga and Castro-Luna, 2010; Selvarajah et al., 2016), and  $\text{ZrO}_2$  (Rong-jun et al., 2015; Lou et al., 2017)) attributes. Metal oxide supports play an important role in catalytic DRM performance. Apart from providing mechanical strength, they increase specific surface area of the catalyst and act as a host for facilitating metal dispersion, thus increasing active metal dispersion (Wang et al., 2018; Abdullah et al., 2017).

Barroso-Quiroga and Castro-Luna (2010) investigated the effect of different ceramic oxide supports, such as  $\text{Al}_2\text{O}_3$ ,  $\text{CeO}_2$ ,  $\text{La}_2\text{O}_3$ , and  $\text{ZrO}_2$ , on the catalytic activity of Ni metal using the incipient wetness impregnation technique for catalytic synthesis. Among supported Ni catalysts, 10% Ni/ $\text{CeO}_2$  exhibited the highest  $\text{CH}_4$  conversion followed by Ni/ $\text{ZrO}_2$  catalyst. However, Ni/ $\text{ZrO}_2$  catalyst was the best catalyst in terms of catalytic stability, with negligible deactivation observed. Lou et al. (2017) also designed a stable  $\text{ZrO}_2$ -supported Ni nanocatalyst system with metal loading of 1–5 wt% using air-stable Ni colloids. Ni/ $\text{ZrO}_2$  catalyst having a 1.1 nm particle dimension reportedly exhibited excellent catalytic stability with TOS and maintained up to 90% initial activity beyond 60 h on-stream. The location of nearly all of the Ni atoms at the interface and perimeter of the  $\text{ZrO}_2$  support could result in easier access to the oxygen generated from activated  $\text{CO}_2$  at the Ni- $\text{ZrO}_2$  interface. Thus, the labile oxygen could facilitate the gasification of surface carbon to CO and prevent Ni/ $\text{ZrO}_2$  catalyst deactivation. The interaction between NiO and various semiconductor metal oxide supports, including  $\text{SiO}_2$ ,  $\text{Al}_2\text{O}_3$ , MgO,  $\text{TiO}_2$ , and  $\text{ZrO}_2$ , was the focus in the DRM study by Rong-jun et al. (2015).  $\text{SiO}_2$ ,  $\text{TiO}_2$ , and  $\text{ZrO}_2$  weakly interact with NiO and hence ease NiO reduction. However, the weak metal support interaction induced quick catalytic deactivation owing to metal agglomeration.  $\text{TiO}_2$ -supported Ni catalyst had the lowest reactant conversions of <5% during 20 h on-stream because of low surface area and weak interaction with NiO, whereas the basic nature of the MgO support attracted acidic  $\text{CO}_2$  adsorption, which in turn gasified surface carbon. Thus, a gradual decrease in the activity of the Ni/MgO catalyst was observed within 50 h and then the catalyst appeared to be stable for 100 h on-stream (Rong-jun et al., 2015).

Ordered mesoporous silica (such as SBA-16 (Zhang et al., 2013), MCM-41 (Xie et al., 2015), and SBA-15 (Omeregbe et al., 2017)) has attracted significant attention from academics and appears to be a promising support because its

large specific surface area, thick framework walls, high thermal stability, and well-ordered hexagonal structure with a narrow pore size distribution yields a supported catalyst with a uniform particle size and high metal dispersion (Zhang et al., 2013; Xie et al., 2015; Omoregbe et al., 2017). Wang et al. (2013) compared different types of silica-based supports on the DRM performance of LaNiO<sub>3</sub> perovskite catalysts, including SiO<sub>2</sub>, mesoporous SBA-15, and MCM-41 materials. Supported catalysts showed higher catalytic activity and stability than those of bare LaNiO<sub>3</sub> catalyst due to a strong metal-support interaction and greater metal dispersion. The initial CH<sub>4</sub> conversion decreased in the following order: LaNiO<sub>3</sub>/MCM-41 > LaNiO<sub>3</sub>/SBA-15 > LaNiO<sub>3</sub>/SiO<sub>2</sub> > LaNiO<sub>3</sub> catalysts. However, the longevity test revealed that the SBA-15 supported LaNiO<sub>3</sub> catalyst was free from graphitic carbon and possessed the highest catalytic stability within 60h at 973K owing to the greater anchoring effect of the SBA-15 mesostructure, resulting in well-dispersed active Ni species. Additionally, the mesoporous structure SBA-15 support was largely undamaged after 60h on-stream, while structural collapse was observed for the MCM-41 support. Cai et al. (2014) also reported that the anchoring effect of mesoporous silica not only contributed to great Ni particle dispersion, inducing remarkable catalytic activity, but also significantly stabilized metallic Ni nanoparticles inside mesoporous channels and prevented them from agglomerating.

Owing to the outstanding oxygen storage capacities and distinctive redox properties of rare earth metal oxides, namely, CeO<sub>2</sub> and La<sub>2</sub>O<sub>3</sub>, these metal oxides have been utilized as supports for reducing carbon deposition (Barroso-Quiroga and Castro-Luna, 2010; Ayodele et al., 2016). Ay and Üner (2015) synthesized Ce-supported Ni, monometallic Co, and bimetallic Ni-Co catalysts using the incipient wetness impregnation approach for DRM evaluation. Both Ni/CeO<sub>2</sub> and Ni-Co/CeO<sub>2</sub> catalysts had excellent interaction between the Ni metal and the CeO<sub>2</sub> support as evidenced in HRTEM analysis, and hence they had higher catalytic activities compared to the Co/CeO<sub>2</sub> catalyst. In the assessment of DRM over Ni/La<sub>2</sub>O<sub>3</sub> catalyst, Li et al. (2017) found that Ni/La<sub>2</sub>O<sub>3</sub> catalyst exhibited outstanding catalytic stability with comparable CH<sub>4</sub> and CO<sub>2</sub> conversions of about 75% at 973K and atmospheric pressure for 50h on-stream. This noteworthy observation was attributed to improved Ni dispersion due to strong metal-support interaction, which thus inhibited Ni sintering and suppressed carbon deposition on the catalyst surface. Additionally, they reported that a complete transformation cycle between the La<sub>2</sub>O<sub>3</sub> and La<sub>2</sub>O<sub>2</sub>CO<sub>3</sub> phases that occurred during DRM was responsible for deposited carbon removal. In particular, CO<sub>2</sub> could adsorb on La<sub>2</sub>O<sub>3</sub> form to generate the intermediate La<sub>2</sub>O<sub>2</sub>CO<sub>3</sub> phase, which in turn reacted with neighboring active surface carbon species to produce CO product and La<sub>2</sub>O<sub>3</sub> form.

Besides single metal oxide supports, mixed metal oxides, such as CeO<sub>2</sub>-Al<sub>2</sub>O<sub>3</sub>, La<sub>2</sub>O<sub>3</sub>-Al<sub>2</sub>O<sub>3</sub> (Charisiou et al., 2016), and MgO-Al<sub>2</sub>O<sub>3</sub> (Zhang et al., 2016), have been recently utilized as a support in DRM catalysts in order to receive synergistic benefits from these compounds. In a study of the DRM

reaction over Ni supported on mixed metal oxides between  $\text{Al}_2\text{O}_3$  and  $\text{CeO}_2$  or  $\text{La}_2\text{O}_3$ , [Charisiou et al. \(2016\)](#) noticed that Ni/CeAl, Ni/LaAl, and Ni/CeLaAl catalysts appreciably improved reactant conversions compared with an unmodified Ni/Al catalyst owing to the high oxygen storage capacity of  $\text{CeO}_2$  and  $\text{La}_2\text{O}_3$  alleviating surface carbon oxidation. Additionally, a longevity test revealed that modified alumina catalysts could constantly retain their catalytic activity over 20h on-stream while the unmodified Ni/Al catalyst experienced catalytic deterioration within 5h.

[Zhang et al. \(2016\)](#) examined a series of Ni/MgO- $\text{Al}_2\text{O}_3$  catalysts (with varying  $\text{Al}_2\text{O}_3$  content from 0 to 45 wt%) synthesized by a two-step hydrothermal approach. NiO reportedly dissolved into the MgO support to form a solid solution, which was difficult to reduce to the active Ni<sup>0</sup> metallic phase. They found that the addition of  $\text{Al}_2\text{O}_3$  to the MgO support could weaken the formation of Mg-Ni-O solid solution and hence alleviate the  $\text{H}_2$  reaction. Nevertheless, the generation of a more spinel-like  $\text{NiAl}_2\text{O}_4$  form at high  $\text{Al}_2\text{O}_3$  loading beyond 15 wt% required a greater reduction temperature than for Ni/MgO catalyst. Additionally, basic site concentration improved with increasing  $\text{Al}_2\text{O}_3$  content in the support mixture and attained an optimum at 15 wt%, which was also the best  $\text{Al}_2\text{O}_3$  loading for the DRM reaction in terms of  $\text{CH}_4$  conversion (52%) and stability due to the formation of a stable and basic  $\text{MgAl}_2\text{O}_4$  phase instead of the undesirable  $\text{MgNiO}_2$  and  $\text{NiAl}_2\text{O}_4$  forms. In the study of Ni/ $\text{MgAl}_2\text{O}_4$  spinel catalysts with various Ni contents from 2.5 to 10% for DRM, [Habibi et al. \(2016\)](#) also found that 5% Ni/ $\text{MgAl}_2\text{O}_4$  exhibited the highest catalytic activity because of high Ni dispersion on the mesoporous  $\text{MgAl}_2\text{O}_4$  support, large BET surface area, low-temperature reducibility, and the strong interaction between the Ni and  $\text{MgAl}_2\text{O}_4$  spinel support.

#### 4.3.2.2 Promoters

Apart from adjusting operational conditions or modifying the structure or composition of catalyst supports, adding small amounts of promoters is an effective way to suppress catalyst deactivation from carbon deposition and metal sintering. Although precious metals exhibit excellent catalytic performance and stability, these metals are preferably employed as promoters due to their high cost and low availability ([Pakhare and Spivey, 2014](#); [Abdullah et al., 2017](#)). In a comparative study of noble metal effect on catalytic activity and carbon deposition for DRM, [Arandiyan et al. \(2014\)](#) prepared various precious metal-doped LaAlNi catalysts (including Pt, Pd, Ru, Rh, and Ir) via the sol-gel method. The addition of noble metal promoters eased the  $\text{H}_2$  reduction of cationic nickel owing to the  $\text{H}_2$ -spillover effect in agreement with the findings from [Jabbour et al. \(2014\)](#). [Arandiyan et al. \(2014\)](#) reported the order of  $\text{CH}_4$  conversion as:  $\text{La}_{0.4}\text{Rh}_{0.6}\text{Al}_{0.2}\text{Ni}_{0.8}\text{O}_3 > \text{La}_{0.4}\text{Ru}_{0.6}\text{Al}_{0.2}\text{Ni}_{0.8}\text{O}_3 > \text{LaAl}_{0.2}\text{Ni}_{0.8}\text{O}_3 > \text{La}_{0.4}\text{Ir}_{0.6}\text{Al}_{0.2}\text{Ni}_{0.8}\text{O}_3 \geq \text{La}_{0.4}\text{Pt}_{0.6}\text{Al}_{0.2}\text{Ni}_{0.8}\text{O}_3 > \text{La}_{0.4}\text{Pd}_{0.6}\text{Al}_{0.2}\text{Ni}_{0.8}\text{O}_3$ . The enhancement of the catalytic performance and stability was ascribed to the low

reduction temperature and the high content of oxygen adspecies on noble metal promoters accelerating surface carbon gasification.

Mahoney et al. (2014) examined the promotional effect of Pt (0.2 wt%) on 15% Ni/Al<sub>2</sub>O<sub>3</sub> and 15% Ni/CeZrO<sub>2</sub> catalysts in a fixed-bed reactor at a stoichiometric CH<sub>4</sub>:CO<sub>2</sub> ratio = 1:1 and 1073 K. The addition of Pt did not significantly affect CH<sub>4</sub> and CO<sub>2</sub> conversions of 15% Ni/Al<sub>2</sub>O<sub>3</sub> catalyst. However, the superior catalytic activity and stability of 0.2% Pt–15% Ni/CeZrO<sub>2</sub> catalyst were attributed to the facilitated oxygen spillover from Pt atoms to the oxygen vacancies in the ceria-zirconia support. Based on density functional theory (DFT) calculations, Gould et al. (2015) found that Pt-promoted Ni catalyst possessed a great resistance to carbon because the presence of Pt atoms weakened the carbon adsorption energy at step edges and increased the carbon diffusion barrier on terraces.

Besides noble metals, rare earth metal oxides (such as CeO<sub>2</sub> and La<sub>2</sub>O<sub>3</sub>) have been widely employed as promoters for Ni-based catalysts due to their basic property and high oxygen storage capacity, which hinders carbonaceous deposition on the catalyst surface and enhances catalytic activity (Usman et al., 2015; Omoregbe et al., 2016). Shamskar et al. (2017) scrutinized the influence of CeO<sub>2</sub> and La<sub>2</sub>O<sub>3</sub> dopants on 25% Ni/Al<sub>2</sub>O<sub>3</sub> catalyst prepared by the ultrasonic-assisted coprecipitation approach. Temperature-programmed oxidation analysis shows that the addition of promoter reduced the amount of accumulated carbon and the 5% CeO<sub>2</sub>–25% Ni/Al<sub>2</sub>O<sub>3</sub> catalyst was stable during 15 h on-stream. The promotional effect of a series of rare-earth elements, namely, Sc, Y, Ce, and Pr on NiMgAl catalysts produced from layered double hydroxides for the DRM reaction was also investigated by Cao et al. (2016). The addition of promoter increased the CH<sub>4</sub> conversion in the order: Ce-promoted > Pr-promoted > Y-promoted > Sc-promoted > unpromoted catalysts. The amount of carbon deposition decreased from 47.22% (unpromoted catalyst) to 33.76% (Ce-doped catalyst). The increased reactant conversion and coke resistance with the addition of a rare-earth promoter were attributed to enhanced surface basicity, the great redox properties, and well-dispersed Ni particles on the catalyst surface. Notably, Ce- and Pr-modified catalysts had higher catalytic activity and carbon resilience compared with other promoted and unpromoted catalysts owing to their fast redox cycling that involved the reversible formation of Ce<sup>3+</sup>/Ce<sup>4+</sup> and Pr<sup>3+</sup>/Pr<sup>4+</sup> redox pairs.

Sarkar et al. (2016) investigated the addition of 0.2 wt% Gd dopant to 5% Ni/ZSM-5 catalyst and found that Gd promotion improved the oxygen atom supply to the adjacent Ni sites and hence oxidized accumulated coke on the catalyst surface. As a result, Gd-doped Ni/ZSM-5 catalyst exhibited a high CH<sub>4</sub> conversion of 83% without noticeable carbon deposition and sintering at 1023 K after 100 h on-stream. Al-Fatesh (2017) also examined the influence of Gd loading from 1 to 5 wt% Gd on the catalytic performance of 10% Ni/Y<sub>2</sub>O<sub>3</sub> catalyst for the DRM reaction. Both CH<sub>4</sub> and CO<sub>2</sub> conversions reportedly increased with increasing Gd loading from 1 to 3 wt% owing to the synergetic effect between

Gd and Ni metals. Metal dispersion was also improved with Gd addition, and the optimal value was obtained at 3 wt% Gd because Gd metal incorporated itself into the pores of the catalyst and inhibited Ni agglomeration. Thus, 3% Gd–10% Ni/Y<sub>2</sub>O<sub>3</sub> catalyst appeared to be the best catalyst in terms of reactant conversions, H<sub>2</sub> yield, and carbon resistance. Boron promoter has recently gained considerable attention for coke resistance in the DRM reaction because, according to DFT calculations from [Xu and Saeys \(2007\)](#), boron atoms effectively suppress surface carbon diffusion into the Ni lattice by preoccupying the octahedral sites of the initial Ni (111) subsurface layer. In the study of boron-promoted Ni/Al<sub>2</sub>O<sub>3</sub> catalyst, [Fouskas et al. \(2014\)](#) found that low boron content (0.6–5.6 wt%) improved Ni dispersion in an Al<sub>2</sub>O<sub>3</sub> support without any changes in textural attributes. Additionally, the total amount of carbonaceous deposits on a B-promoted catalyst was about 74%–86% lower than on unpromoted catalyst.

[Table 4.9](#) summarizes the catalytic performance of various nonnoble metal-based catalysts employing various support and promoter types. In order to facilitate the comparison among the catalysts used, the experimental conditions, including feed composition, reaction temperature, and gas hourly space velocity (GHSV), are also listed. In addition, the initial and final reactant conversions are given to justify catalytic stability. In fact, the estimated degree of catalyst deactivation based on CH<sub>4</sub> conversion is also summarized, together with the H<sub>2</sub>/CO ratio.

#### 4.3.2.3 DRM Kinetic Models

Fundamentally understanding the intrinsic mechanistic DRM pathways and determining the kinetic parameters based on the best-fit kinetic model are essential for optimizing catalyst synthesis and subsequent reactor design for commercialized applications in industry. The typical kinetic models commonly implemented in the DRM reaction are the power law, Eley Rideal (ER), and Langmuir Hinshelwood-Hougen Watson (LHHW) models. Among these main kinetic models, the empirical power law model is regarded as the simplest one capable of generating approximately estimated values for associated reaction parameters. The empirical power law model for the DRM reaction is given in Eq. (4.16).

$$-r_{\text{CH}_4} = kP_{\text{CH}_4}^{\alpha} P_{\text{CO}_2}^{\beta} \quad (4.16)$$

where  $P_i$  is the partial pressure of component  $i$  ( $i$ : CH<sub>4</sub> or CO<sub>2</sub>) and  $k$  is the apparent rate constant. Additionally,  $\alpha$  and  $\beta$  are reaction orders varying with the type of catalyst while  $-r_{\text{CH}_4}$  is the reaction rate of CH<sub>4</sub>.

Although the power law model has been widely employed in many studies ([Pakhare and Spivey, 2014](#); [Kathiraser et al., 2015](#)) for roughly computing the kinetic parameters because of its simplicity and because there is no requirement to understand the mechanistic reaction pathways (see summary in [Table 4.10](#)),

**TABLE 4.9** Bibliographic Listing of Catalytic Performance for Recently Employed Catalysts in DRM Reaction

Catalysts	CH <sub>4</sub> /CO <sub>2</sub> Ratio	T (K)	GHSV (L g <sub>cat</sub> <sup>-1</sup> h <sup>-1</sup> )	Initial Performance			TOS <sup>a</sup> (h)	Final Performance			D <sup>b</sup> (%)	References
				CH <sub>4</sub> Conversion (%)	CO <sub>2</sub> Conversion (%)	H <sub>2</sub> /CO Ratio		CH <sub>4</sub> Conversion (%)	CO <sub>2</sub> Conversion (%)	H <sub>2</sub> /CO Ratio		
<i>Supported catalysts</i>												
NiO/SiO <sub>2</sub>	1.0/1.0	1023	–	86.9	89.8	–	100	74.7	80.4	–	7.5	Zhang et al. (2015)
NiO/TiO <sub>2</sub>	1.0/1.0	1023	–	4.1	3.2	–	20	1.4	4.3	–	65.9	Zhang et al. (2015)
NiO/Al <sub>2</sub> O <sub>3</sub>	1.0/1.0	1023	–	77.5	57.8	–	30	76.8	53.3	–	0.1	Zhang et al. (2015)
NiO/ZrO <sub>2</sub>	1.0/1.0	1023	–	88.5	88.8	–	30	16.7	21.8	–	81.1	Zhang et al. (2015)
NiO/MgO	1.0/1.0	1023	–	88.1	90.1	–	100	74.3	76.5	–	15.7	Zhang et al. (2015)
Ni/CZ/SBA-15	1.0/1.0	873	20.0	49.6	66.4	0.76	28	41.9	58.0	0.24	15.5	Albarazi et al. (2013)
Ni/CeO <sub>2</sub> -Al <sub>2</sub> O <sub>3</sub>	–	973	–	79.4	–	0.93	80	76.9	–	0.91	3.1	Wang et al. (2014)
Ni/MgAl <sub>2</sub> O <sub>4</sub>	1.0/1.0	973	18.0	74.4	83.3	–	15	70.6	81.2	–	5.1	Habibi et al. (2016)

Ni/MgAl <sub>2</sub> O <sub>4</sub>	1.0/1.0	973	12.0	57.7	–	–	5	56.3	–	–	2.4	Zarei et al. (2016)
Ni-MgO-Al <sub>2</sub> O <sub>3</sub>	1.0/1.0	973	180.0	76.1	82.3	0.96	12	71.4	79.8	0.92	6.2	Akbari et al. (2017)
Ni/MgO-Al <sub>2</sub> O <sub>3</sub>	1.0/1.0	923	60.0	46.5	57.1	0.64	10	40.5	52.0	0.63	12.9	Zhang et al. (2016)
Mg <sub>0.8</sub> Ni <sub>0.2</sub> Al <sub>2</sub> O <sub>4</sub>	1.0/1.0	973	18.0	74.0	82.5	–	–	67.2	78.6	–	9.2	Habibi et al. (2017)
<i>Promoted catalysts</i>												
Pt-Ni/CeZrO <sub>2</sub>	0.5/0.5	1073	120.0	94.2	96.2	0.85	15	93.5	95.8	0.91	0.7	Mahoney et al. (2014)
Gd-promoted Ni/ZSM-5	1.0/1.0	1023	50.0	85.0	–	0.98	1	–	–	–	–	Sarkar et al. (2016)
Sm-promoted Ni/ZSM-5	1.0/1.0	1023	50.0	84.0	–	0.92	1	–	–	–	–	Sarkar et al. (2016)
Gd-promoted Ni/Y <sub>2</sub> O <sub>3</sub>	1.0/1.0	973	8.0	85.7	83.6	–	6	83.4	81.1	–	2.7	Al-Fatesh (2017)
Ce-promoted Ni/Al <sub>2</sub> O <sub>3</sub>	1.0/1.0	973	12.0	59.9	78.2	0.78	5	58.9	78.3	0.77	1.7	Shamskar et al. (2017)
La-promoted Ni/Al <sub>2</sub> O <sub>3</sub>	1.0/1.0	973	12.0	56.4	76.7	0.76	5	54.6	76.6	0.75	3.2	Shamskar et al. (2017)
Zr-promoted Ni/Al <sub>2</sub> O <sub>3</sub>	1.0/1.0	973	12.0	53.4	74.0	0.76	5	51.8	74.2	0.74	3.0	Shamskar et al. (2017)

*Continued*

**TABLE 4.9 Bibliographic Listing of Catalytic Performance for Recently Employed Catalysts in DRM Reaction — cont'd**

Catalysts	CH <sub>4</sub> /CO <sub>2</sub> Ratio	T (K)	GHSV (L g <sub>cat</sub> <sup>-1</sup> h <sup>-1</sup> )	Initial Performance			TOS (h)	Final Performance			D (%)	References
				CH <sub>4</sub> Conversion (%)	CO <sub>2</sub> Conversion (%)	H <sub>2</sub> /CO Ratio		CH <sub>4</sub> Conversion (%)	CO <sub>2</sub> Conversion (%)	H <sub>2</sub> /CO Ratio		
Mo-promoted Ni/Al <sub>2</sub> O <sub>3</sub>	1.0/1.0	873	200.0	25.6	33.8	0.64	7	22.1	30.2	0.60	13.7	Yao et al. (2017)
B-promoted Ni/Al <sub>2</sub> O <sub>3</sub>	1.0/1.0	973	30.0	–	–	–	24	51.4	61.9	–	–	Fouskas et al. (2014)
<i>Bimetallic catalysts</i>												
Co-Zr/AC	1.0/1.0	873	7.2	91.7	91.2	–	45	88.9	89.1	–	3.1	Zhang et al. (2015)
Co-Ni/Al <sub>2</sub> O <sub>3</sub> -MgO	1.0/1.0	1123	24.0	97.3	99.1	0.97	20	92.3	95.4	0.97	5.2	Abdollahifar et al. (2016)
Pd-Ni/Al <sub>2</sub> O <sub>3</sub>	1.0/1.0	1023	8.0	87.0	94.2	1.06	100	84.7	83.3	1.03	2.6	Ma et al. (2016)
Co <sub>3</sub> Mo <sub>3</sub> N	1.0/1.0	1073	6.0	96.9	98.9	0.93	50	86.5	98.4	0.83	10.7	Fu et al. (2017)
Co-Ni/Al <sub>2</sub> O <sub>3</sub>	1.0/1.0	873	–	23.4	30.9	0.58	180	15.7	17.7	0.46	32.9	Ray et al. (2017)

<sup>a</sup>Time-on-stream (TOS) is defined as the period of stability measurements at a fixed reaction temperature.

<sup>b</sup>Degree of catalyst deactivation, D (%) =  $[1 - (\text{Final CH}_4 \text{ conversion} / \text{Initial CH}_4 \text{ conversion})] \times 100\%$ .

**TABLE 4.10** Summary of Kinetic Parameters Derived From Power Law Models of DRM Over Different Catalysts

Catalysts	Temperature (K)	Activation Energy, $E_a$ (kJ/mol)	Reaction Order			References
			$\alpha$	$\beta$	$\text{CO}_2$	
0.3%Pt–10%Ni/Al <sub>2</sub> O <sub>3</sub>	853–893	CH <sub>4</sub> 112.5	CH <sub>4</sub> 1.0	CO <sub>2</sub> 0.9	Özkara-Aydınoglu and Aksoylu (2013)	
0.2%Pt–15%Ni/Al <sub>2</sub> O <sub>3</sub>	853–893	111.3	1.1	1.4	Wang et al. (2014)	
Co/La <sub>2</sub> O <sub>3</sub>	923–1023	96.4	3.7	0.4	Ayodele et al. (2016)	
SmCoO <sub>3</sub>	973–1073	41.0	1.2	0.3	Osazuwa et al. (2017)	
Co/Sm <sub>2</sub> O <sub>3</sub>	923–1023	88.6	3.1	0.2	Ayodele et al. (2017)	
La <sub>2-x</sub> Sr <sub>x</sub> NiO <sub>4</sub>	633–713	41.8	0.9–0.4	0.2–0.1	Pichas et al. (2010)	
13.5%Ni–2%K/CeO <sub>2</sub> - Al <sub>2</sub> O <sub>3</sub>	823–1073	113.8	0.9–1.0	0.3–0.5	Pechimuthu et al. (2006)	

the power law model may not be applicable and accurate for a wide range of reactant partial pressure (Pakhare and Spivey, 2014; Kathiraser et al., 2015). Nevertheless, this empirical model can be effectively used for initially guessing the overall activation energy and power constants of each reactant for comparison among catalysts used in the literature.

Table 4.10 summarizes the estimated CH<sub>4</sub> activation energy and reaction orders obtained from power law models recently reported in the literature for several catalysts. Özkara-Aydinoğlu and Aksoylu (2013) fitted the experimental data for DRM on Pt-Ni/Al<sub>2</sub>O<sub>3</sub> catalysts to a power law model and found that the reaction orders of CH<sub>4</sub> and CO<sub>2</sub> varied from 1.0 to 1.1 and 0.9 to 1.4 in this order depending on the Pt and Ni loading. For 0.2% Pt–15% Ni/Al<sub>2</sub>O<sub>3</sub> catalyst, the higher reaction order for CO<sub>2</sub> than for CH<sub>4</sub> suggests a greater reliance on the CO<sub>2</sub> partial pressure for surface carbon gasification. However, at higher Pt content (0.3% Pt–10% Ni/Al<sub>2</sub>O<sub>3</sub>), the CO<sub>2</sub> dependency was reduced and CH<sub>4</sub> appeared to be the dominant component affecting the reaction rate, because higher Pt content enhanced the oxygen utilization for removing deposited carbon. As seen in Table 4.10, the CH<sub>4</sub> reaction order was superior to that of CO<sub>2</sub> for most catalysts, suggesting that CH<sub>4</sub> adsorption on the catalyst surface dominated the DRM reaction.

As discussed above, the power law models do not reflect the intrinsic DRM reaction steps occurring on the catalyst surface. Thus, in order to thoroughly understand various complex mechanistic DRM schemes, ER and LHHW models are normally employed, together with statistical criteria and thermodynamic consistency (Abdullah et al., 2017), for assessing the adequacy of the fitting of experimental data to the mechanistic-based kinetic models. Özkara-Aydinoğlu and Aksoylu (2013) investigated Pt-Ni/Al<sub>2</sub>O<sub>3</sub> catalyst for the DRM reaction and fitted their experimental data on the CH<sub>4</sub> consumption rate into eight ER and LHHW kinetic models derived from various mechanistic pathways with different rate-determining steps (RDS). Based on the squared error from nonlinear regression, they deduced that the ER model (see Eq. 4.17 in Table 4.11) in which the reaction between molecularly adsorbed CO<sub>2</sub> and CH<sub>4</sub> in the gas phase is the RDS, was the model that provided the best fit.

In kinetic studies of Pt- and Ru-doped TiO<sub>2</sub> catalysts, Singh and Madras (2016) performed an in situ FTIR analysis during the DRM reaction and found that CH<sub>4</sub> adsorbed on the catalyst surface while the absence of adsorbed CO<sub>2</sub> species on the metal or support surfaces was evident. Hence, an ER model (see Eq. 4.18 in Table 4.11) in which CH<sub>4</sub> adsorbs molecularly, followed by CH<sub>4</sub> dissociative adsorption as RDS (rate-determining step) while CO<sub>2</sub> exists in the gas phase, was proposed to forecast the experimental reaction rate.

Ayodele et al. (2017) examined the CH<sub>4</sub> reaction rate over Co/La<sub>2</sub>O<sub>3</sub> catalyst in six different LHHW models derived from both single-site (adsorption of CH<sub>4</sub> and CO<sub>2</sub> reactants on the same active site) and dual-site (CH<sub>4</sub> and CO<sub>2</sub> favorably adsorbed on two nonidentical sites on active metal and support) mechanisms. They discovered that the experimental data on the CH<sub>4</sub>

**TABLE 4.11** Representative ER and LHHW Kinetic Rate Models for DRM Over Different Catalysts

Catalysts	Assumption	Mechanism	Kinetic Model	Equations	References
Pt-Ni/ Al <sub>2</sub> O <sub>3</sub>	Reaction of molecularly adsorbed CO <sub>2</sub> with CH <sub>4</sub> in gas phase as RDS <sup>a</sup>	$\text{CO}_2 + \text{X} \xrightleftharpoons{K_1} \text{CO}_2 - \text{X}$ $\text{CO}_2 - \text{X} + \text{CH}_4 \xrightarrow{k_2} 2\text{CO} + 2\text{H}_2 + \text{X} \quad (\text{RDS}^*)$	$-r_{\text{CH}_4} = \frac{k_2 K_1 P_{\text{CH}_4} P_{\text{CO}}}{(1 + K_1 P_{\text{CO}_2})}$	(4.17)	Özkara-Aydinoğlu and Aksoylu (2013)
Pt/TiO <sub>2</sub>	Single-site CH <sub>4</sub> molecular adsorption with CH <sub>4</sub> dissociation as RDS	$\text{CH}_4 + \text{X} \xrightleftharpoons{K_1} \text{CH}_4 - \text{X}$ $\text{CH}_4 - \text{X} \xrightarrow{k_2} \text{C} - \text{X} + 2\text{H}_2 \quad (\text{RDS})$ $\text{X} - \text{C} + \text{CO}_2 + \text{X} \xrightleftharpoons{K_3} 2\text{X} - \text{CO}$ $2\text{X} - \text{CO} \xrightleftharpoons{K_4} 2\text{X} + 2\text{CO}$	$-r_{\text{CH}_4} = \frac{k_2 K_1 K_3 K_4 P_{\text{CH}_4} P_{\text{CO}_2}}{(1 + K_1 P_{\text{CH}_4}) K_3 K_4 P_{\text{CO}_2} + K_3 \sqrt{K_4} P_{\text{CO}} + P_{\text{CO}}^2}$	(4.18)	Singh and Madras (2016)
Co/La <sub>2</sub> O <sub>3</sub>	Dual-site CH <sub>4</sub> and CO <sub>2</sub> associative adsorption with bimolecular surface reaction as RDS	$\text{CH}_4 + \text{X}_1 \xrightleftharpoons{K_1} \text{CH}_4 - \text{X}_1$ $\text{CO}_2 + \text{X}_2 \xrightleftharpoons{K_2} \text{CO}_2 - \text{X}_2$ $\text{CH}_4 - \text{X}_1 + \text{CO}_2 - \text{X}_2 \xrightarrow{k_3} 2\text{H}_2 + 2\text{CO} + \text{X}_1 + \text{X}_2 \quad (\text{RDS})$	$-r_{\text{CH}_4} = \frac{k_3 P_{\text{CH}_4} P_{\text{CO}_2}}{(1 + K_1 P_{\text{CH}_4})(1 + K_2 P_{\text{CO}_2})}$	(4.19)	Ayodele et al. (2016)

Continued

**TABLE 4.11** Representative ER and LHHW Kinetic Rate Models for DRM Over Different Catalysts — cont'd

Catalysts	Assumption	Mechanism	Kinetic Model	Equations	References
Ni-Rh/ Al <sub>2</sub> O <sub>3</sub>	Dual-site mechanism and surface reaction between adsorbed CH <sub>3</sub> and CO <sub>2</sub> species as RDS	$\text{CH}_4 + \text{X}_1 \xrightleftharpoons{K_1} \text{X}_1 - \text{CH}_3 + \frac{1}{2} \text{H}_2$ $\text{CO}_2 + \text{X}_2 \xrightleftharpoons{K_2} \text{CO}_2 - \text{X}_2$ $\text{X}_1 - \text{CH}_3 + \text{CO}_2 - \text{X}_2 \xrightarrow{K_3} 2\text{CO} + \frac{3}{2} \text{H}_2 + \text{X}_1 + \text{X}_2 \quad (\text{RDS})$	$-r_{\text{CH}_4} = \frac{k_3 K_1 K_2 \frac{P_{\text{CH}_4} P_{\text{CO}_2}}{P_{\text{H}_2}^{0.5}} \frac{P_{\text{H}_2}^{1.5} P_{\text{CO}_2}^2}{K_{\text{ref}}}}{1 + \frac{P_{\text{CH}_4}}{P_{\text{H}_2}^{0.5} K_1} + P_{\text{CO}_2} K_2}$	(4.20)	Barroso-Quiroga and Castro-Luna (2007)
Co-Ni/ Al <sub>2</sub> O <sub>3</sub>	Dual-site LHHW mechanism in which surface reaction between adsorbed carbon and oxygen species is RDS	$\text{CH}_4 + 2\text{X}_1 \leftrightarrow \text{CH}_3 - \text{X}_1 + \text{H} - \text{X}_1$ $\text{CH}_3 - \text{X}_1 + \text{X}_1 \leftrightarrow \text{CH}_y - \text{X}_1 + \text{H} - \text{X}_1; \quad 1 \leq y \leq 3$ $\text{CH} - \text{X}_1 + \text{X}_1 \leftrightarrow \text{C} - \text{X}_1 + \text{H} - \text{X}_1$ $\text{CO}_2 + 2\text{X}_2 \leftrightarrow \text{CO} - \text{X}_2 + \text{O} - \text{X}_2$ $\text{C} - \text{X}_1 + \text{O} - \text{X}_2 \xrightarrow{k_{\text{rxn}}} \text{CO} - \text{X}_2 + \text{X}_1 \quad (\text{RDS})$ $2\text{H} - \text{X}_1 \leftrightarrow \text{H}_2 + 2\text{X}_1$ $\text{CO} - \text{X}_2 \leftrightarrow \text{CO} + \text{X}_2$ $\text{H} - \text{X}_1 + \text{O} - \text{X}_2 \leftrightarrow \text{OH} - \text{X}_2 + \text{X}_1$ $\text{H} - \text{X}_1 + \text{OH} - \text{X}_2 \leftrightarrow \text{H}_2\text{O} + \text{X}_1 + \text{X}_2$	$-r_{\text{CH}_4} = \frac{k_{\text{rxn}} \sqrt{P_{\text{CH}_4}} \sqrt{P_{\text{CO}_2}}}{(1 + \sqrt{K_{\text{CH}_4} P_{\text{CH}_4}}) (1 + \sqrt{K_{\text{CO}_2} P_{\text{CO}_2}})}$	(4.21)	Foo et al. (2011)

<sup>a</sup>RDS is a rate-determining step with X being available active site.

consumption rate at different reactant partial pressures from 5 to 50 kPa, and different reaction temperatures from 923 to 1023 K, were sufficiently captured by a dual-site LHHW model (see Eq. 4.19 in Table 4.11) with surface reaction between molecularly adsorbed  $\text{CH}_4$  and  $\text{CO}_2$  species as RDS. This model satisfied both statistical and thermodynamic criteria with a high correlation coefficient ( $>0.95$ ). Other dual-site LHHW models with detailed mechanistic steps are also summarized in Table 4.11.

#### 4.3.2.4 Conclusions and Outlook

DRM is a promising green technology to produce a syngas mixture appropriate for downstream production of synthetic long-chained hydrocarbons via Fischer-Tropsch synthesis. However, the DRM technology is still impractical for implementation at an industrial scale because the highly endothermic nature of DRM requires excessive energy consumption, leading to high operating and investment costs. In addition, the inevitably severe catalyst deactivation induced by carbon deposition and metal sintering at high reaction temperature is another limitation of DRM. The synergistic effect of promoters and supports on catalytic attributes, including metal dispersion, extent of metal-support interaction, and crystallite size, has been extensively studied to improve catalytic performance and stability. The use of appropriate supports or promoters possessing a mesoporous structure and basic or redox properties help prevent the catalyst from deteriorating by carbonaceous deposition and sintering.

Power law, ER, and LHHW models are the three standard DRM kinetic models. The empirical power law models do not explain the complex and multi-step pathways of the DRM reaction, but the reaction orders could indicate the dominance or important role of reactant partial pressure on overall catalytic activity. A large number of mechanistic-based ER and LHHW models derived from single-site or dual-site mechanisms with various RDS have been proposed for capturing the  $\text{CH}_4$  consumption rate.

Apart from utilizing suitable supports and promoters to formulate carbon-resistant catalysts, carbonaceous deposition may be suppressed by cofeeding a small amount of oxidizing reactants, namely,  $\text{H}_2\text{O}$  and  $\text{O}_2$ , to the  $\text{CH}_4$  and  $\text{CO}_2$  reactant mixture. In fact, bi-reforming (or combined steam and DRM) and oxidative DRM (referring to DRM with the corresponding addition of  $\text{H}_2\text{O}$  and  $\text{O}_2$  reactants) have recently been considered as alternative approaches to inhibit coke deposition. In the presence of these oxidizing agents, surface carbon can be easily gasified to gaseous products, thus keeping the catalyst surface free from carbonaceous species. Additionally, these reforming processes are capable of generating syngas with desirable and flexible  $\text{H}_2/\text{CO}$  ratios for downstream processing via manipulation of reactant composition. Future investigations into bi-reforming and oxidative DRM in terms of catalyst recipe and kinetic modeling could be considered to optimize the efficiency of reforming processes for large-scale production.

## 4.4 TRI-REFORMING OF METHANE

### 4.4.1 Thermodynamic Equilibrium Aspect

In a given landfill gas, some quantity of oxygen is usually present, possibly up to 5 vol%. It is meaningful to be able to reform a purified landfill containing again oxygen. Fig. 4.11 shows the thermodynamic equilibrium of a mixture containing 51.3% CH<sub>4</sub>, 25.6% CO<sub>2</sub>, 20.5% H<sub>2</sub>O, and 2.6% O<sub>2</sub> (molar percentage, or 2 mol of CH<sub>4</sub>, 1 mol of H<sub>2</sub>O, 1 mol of CO<sub>2</sub>, and 0.1 mol of O<sub>2</sub>) at atmospheric pressure. This mixture corresponds to a stoichiometric reaction of CH<sub>4</sub> with the three oxidants, according to Eqs. (4.1), (4.5), (4.7) in Table 4.2. Oxygen is completely consumed in the temperature range studied. Methane is gradually consumed above 350°C and it practically disappears above 850°C (>98%). Solid carbon can be nearly eliminated above 800°C and it is very important for avoiding the catalyst deactivation by coke deposition. Water is permanently present as a byproduct due to the WGS. Finally, H<sub>2</sub> and CO are formed as the main products, with high selectivity above 800°C, and the molar ratio of H<sub>2</sub>/CO is close to 1.65 within 800–1000°C, which is interesting for hydrocarbon synthesis via the Fisher-Tropsch process. Thus, it is recommended to perform tri-reforming above 800°C.

Fig. 4.12 shows the thermodynamic equilibrium of a mixture containing 43.5% CH<sub>4</sub>, 21.7% CO<sub>2</sub>, 32.6% H<sub>2</sub>O, and 2.2% O<sub>2</sub> (molar percentage, or

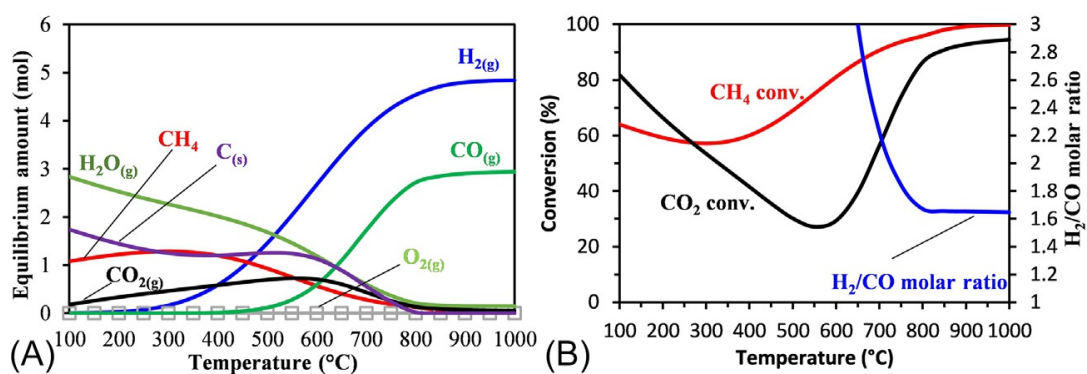


FIG. 4.11 Thermodynamic Equilibrium of the Mixture Containing 2 mol of CH<sub>4</sub>, 1 mol of H<sub>2</sub>O, 1 mol of CO<sub>2</sub>, and 0.1 mol of O<sub>2</sub>.

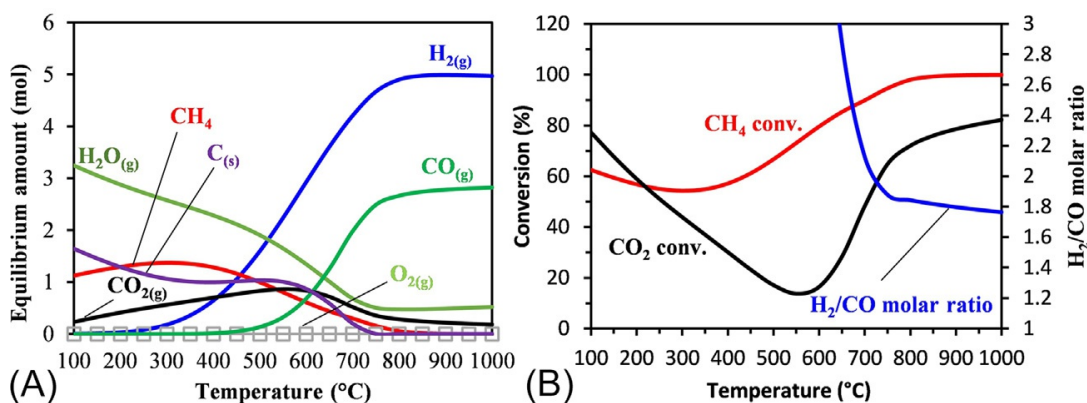


FIG. 4.12 Thermodynamic equilibrium of the mixture containing 2 mol of CH<sub>4</sub>, 1.5 mol of H<sub>2</sub>O, 1 mol of CO<sub>2</sub> and 0.1 mol of O<sub>2</sub>.

2 mol of CH<sub>4</sub>, 1.5 mol of H<sub>2</sub>O, 1 mol of CO<sub>2</sub>, and 0.1 mol of O<sub>2</sub>) at atmospheric pressure. This mixture contains a slight excess of oxidants to methane, or the molar ratio of (H<sub>2</sub>O+CO<sub>2</sub>+O<sub>2</sub>)/CH<sub>4</sub> of this mixture is equal to 2.1/2. The behavior of this system is similar to the system presented in Fig. 4.11. It is worth noting that adding more water avoids early solid carbon formation as of 750°C. At 800°C, the methane conversion can reach 98.1% with high selectivity in H<sub>2</sub> and CO, and the molar ratio of H<sub>2</sub>/CO can reach 1.87. However, both H<sub>2</sub>O and CO<sub>2</sub> are present in large excess and can negatively impact the final energy balance of the reforming process.

#### 4.4.2 Catalysts for Methane Tri-Reforming

The TRM process has been regarded as a synergetic combination technique consisting of endothermic steam reforming of methane, DRM, and exothermic partial oxidation of methane. As a heterogeneous catalytic reforming process, Ni-based catalysts are widely used in TRM due to their low cost, high availability, and capability of C-H bond cleavage. Support and promoter are the main components of industrial Ni-based catalysts and substantially influence the catalytic performance in terms of reactant conversions, selectivity, and stability in harsh TRM reaction conditions. The effect of various supports and promoters on TRM catalysts will be discussed thoroughly in the following sections.

##### 4.4.2.1 Catalyst Supports

As in steam reforming and dry reforming processes, the utilization of supports for dispersing active metals and providing mechanical strength for catalysts also plays a crucial role in TRM in terms of catalytic activity, product selectivity, and stability. A wide range of supports has been examined for TRM based on several main selection standards and their intrinsic nature (Song and Pan, 2004; García-Vargas et al., 2014). For instance, because CO<sub>2</sub> is one of the reactants in TRM, supports having a basic character or high oxygen storage capacity could enhance CO<sub>2</sub> adsorption and hence increase CO<sub>2</sub> conversion (Song and Pan, 2004).

Song and Pan (2004) investigated the effect of both single-metal oxides, namely, CeO<sub>2</sub>, ZrO<sub>2</sub>, MgO, and Al<sub>2</sub>O<sub>3</sub>, and mixed-metal oxides, including CeO<sub>2</sub>-ZrO<sub>2</sub> with a Ce:Zr atomic ratio = 3, on the TRM catalytic performance of Ni catalysts prepared via the wet impregnation method. They observed that high CH<sub>4</sub> (≥97%) and CO<sub>2</sub> (about 80%) conversions were attained on supported Ni catalysts with desirable H<sub>2</sub>/CO ratios ranging from 1.5 to 2.0 at a reaction temperature of 1073–1123 K and atmospheric pressure. In addition, unlike DRM reaction, TPO measurements for the deposited carbon content on the catalysts used indicate that, except for the Ni/ZrO<sub>2</sub> catalyst with a small quantity of carbonaceous carbon (1.34 wt%), carbon deposition was not present on other Ni-based catalysts. They also found that the capability of CO<sub>2</sub> consumption over different supported catalysts was strongly reliant on the extent of

interaction between metal and support. The order of CO<sub>2</sub> conversion in TRM was reported as: Ni/MgO > Ni/MgO/CeZrO > Ni/CeO<sub>2</sub> ≈ Ni/ZrO<sub>2</sub> ≈ Ni/Al<sub>2</sub>O<sub>3</sub> > Ni/CeZrO. Among the supported Ni catalysts, the greater CO<sub>2</sub> conversion on the Ni/MgO and Ni/MgO/CeZrO catalysts was attributed to the stronger interaction of MgO and CO<sub>2</sub>, as well as more Ni and MgO interface arising from the formation of NiO/MgO solid solution.

In the study of support influence on Ni catalysts for TRM, [García-Vargas et al. \(2014\)](#) synthesized five different Ni catalysts dispersed on various supports, including  $\gamma$ -Al<sub>2</sub>O<sub>3</sub>, yttria-stabilized zirconia (YSZ), yttria-stabilized zirconia calcined in an oxygen-poor environment (YSZ-O<sub>2</sub>), CeO<sub>2</sub>, and silicon carbide ( $\beta$ -SiC) ([García-Vargas et al., 2014](#)). Gamma-alumina was selected as a support due to its mechanical strength and thermal stability under the high reaction temperature required for TRM, while ZrO<sub>2</sub>-based supports reportedly possessed high thermal resistance and ionic conductivity for reforming processes because of their crystal surface defects in which oxygen reactant could easily be activated, and hence enhance reactivity ([Bellido and Assaf, 2009](#)). Apart from high thermal conductivity and mechanical strength, SiC has chemical inertness and low specific weight, which are appropriate properties for being supports of the endothermic TRM reaction ([García-Vargas et al., 2014](#)). [García-Vargas et al. \(2014\)](#) reported that CeO<sub>2</sub> and  $\beta$ -SiC materials appeared to be the best catalytic supports for the TRM process. In fact, CeO<sub>2</sub>- and  $\beta$ -SiC-supported Ni catalysts exhibited the highest CH<sub>4</sub> reaction rate without considerable deactivation. Ni/CeO<sub>2</sub> catalyst yielded the lowest H<sub>2</sub>/CO ratio and this observation was attributed to the high basicity of the CeO<sub>2</sub> support, which enhanced CO<sub>2</sub> adsorption to initiate more of the methane dry reforming reaction. Among supported catalysts, Ni/Al<sub>2</sub>O<sub>3</sub> catalyst showed the lowest CH<sub>4</sub> and CO<sub>2</sub> conversions owing to the formation of the NiAl<sub>2</sub>O<sub>4</sub> phase. In addition, the catalytic performance of Ni/YSZ-O<sub>2</sub> catalyst was superior to that of Ni/YSZ catalyst because the calcination conditions of Ni/YSZ-O<sub>2</sub> catalyst resulted in a better NiO reducibility and greater number of oxygen vacancies on the support surface.

Based on the aforementioned important characteristics of supports for TRM catalyst design, composite oxides, such as MgO-TiO<sub>2</sub> ([Jiang et al., 2007](#)) and MgO-ZrO<sub>2</sub> ([Walker et al., 2012](#)), have been developed as promising supports as these materials also have high surface oxygen vacancies and great basic site concentration, which could contribute to increase carbonaceous gasification. [Jiang et al. \(2007\)](#) investigated Mg<sub>x</sub>Ti<sub>1-x</sub>O composite oxides (with  $0 \leq x \leq 1$ ) as supports for impregnation of nickel nitrate. TRM longevity runs were conducted in a continuous-flow fixed-bed reactor at 1123 K and 1 MPa for 50 h. The activity of Ni/MgO, Ni/Mg<sub>0.25</sub>Ti<sub>0.75</sub>O and Ni/TiO<sub>2</sub> catalysts declined within 6 h on-stream while high catalytic stability was observed for the Ni/Mg<sub>0.75</sub>Ti<sub>0.25</sub>O and Ni/Mg<sub>0.5</sub>Ti<sub>0.5</sub>O catalysts. Catalyst deactivation was reportedly induced by the re-oxidation of the Ni metallic phase to the inactive NiO phase or support

phase transformation at high temperature. There was no graphitic carbon or carbon fiber detected in XRD and SEM measurements for Ni/Mg<sub>0.75</sub>Ti<sub>0.25</sub>O and Ni/Mg<sub>0.5</sub>Ti<sub>0.5</sub>O catalysts. The authors deduced that the moderate metal-support interaction and the right ability to be reduced contributed to the high stability of Ni/Mg<sub>0.75</sub>Ti<sub>0.25</sub>O and Ni/Mg<sub>0.5</sub>Ti<sub>0.5</sub>O catalysts.

Walker et al. (2012) studied the effect of support composition, metal loading, and preparation method on the catalytic performance of Ni-MgO-(Ce, Zr)O<sub>2</sub> composite catalysts for TRM. They discovered that implementing even more Ce:Zr ratio could yield an increase in oxygen mobility and redox attributes, which in turn allow the movement of oxygen atoms to suitable sites for removing surface carbonaceous species. In addition, a greater H<sub>2</sub> yield and production rate were observed during TRM over catalyst with a Ni:Mg ratio of 1:1. As the Ni:Mg metal ratio was about unity, a greater number of interfaces between the Ni and Mg phases were formed. Because MgO has a basic nature, preferably attracting CO<sub>2</sub> adsorption, more Ni and Mg interfaces could facilitate CO<sub>2</sub> dissociative adsorption, and consequently, the oxygen mobility could oxidize the adsorbed carbon species originating from CH<sub>4</sub> decomposition on the Ni surface.

Singha et al. (2016) modified CeO<sub>2</sub>-ZrO<sub>2</sub> nanoporous composite with the addition of MgO for synthesizing a Ni nanocluster catalyst for TRM. MgO addition was reportedly coke-resistant and sintering-resistant in TRM reaction conditions. The 5% Ni-MgCeZr composite catalyst showed a highly stable catalytic activity, with high CH<sub>4</sub> conversion (95%) and an ideal H<sub>2</sub>/CO ratio of about 2 for TRM, without any deactivation over 100h on-stream. They attributed this outstanding catalytic performance to the synergetic effects of the various metal oxides employed. In fact, ZrO<sub>2</sub> enhanced the thermal stability of the catalyst while the interaction between MgO and Ce<sub>x</sub>Zr<sub>1-x</sub>O<sub>2</sub> metal oxides improved the dispersion of Ni particles. In addition, a CeO<sub>2</sub>-ZrO<sub>2</sub> solid solution could increase the oxygen storage capacity, facilitating the carbon removal process due to high surface oxygen vacancies and great oxygen mobility in the lattice. Pino et al. (2014) also reported similar findings for TRM over Ni-based catalysts supported on La-Ce-O mixed oxides. In this study, a series of La-Ce-O mixed oxide—supported Ni catalysts with various Ni loadings was prepared using the combustion technique. The highest catalytic activity was evident for Ce<sub>0.7</sub>La<sub>0.2</sub>Ni<sub>0.1</sub>O<sub>2-δ</sub> catalyst, with no detectable carbon deposition observed in a SEM image after 150h on-stream. After the prereduction step, the formation of LaO<sub>x</sub> species increased the d-electron density of Ni atoms, which in turn hindered carbonaceous deposition on the catalyst surface. The authors concluded that the high catalytic activity was associated with the interaction between nickel-lanthana and surface oxygen vacancies of CeO<sub>2</sub>, which resulted in rising metal dispersion. However, at high active metal and La<sub>2</sub>O<sub>3</sub> contents, the observed catalytic deterioration with TOS was attributed to re-oxidation of the Ni<sup>0</sup> metallic phase, metal sintering, and surface coverage by excessive lanthana species.

#### 4.4.2.2 Promoters

Because the TRM process is a complex heterogeneous catalytic reaction involving the concomitant presence of three main catalytic reactions (including methane steam reforming, methane dry reforming, and methane partial oxidation), apart from metal oxide supports, the role of promoter addition to a TRM catalyst is essential for maximizing catalytic performance, product yield, and catalytic stability with TOS in drastic operation conditions. As a typical reforming process, rare-earth metal oxides are also employed as promoters for Ni-based catalysts in the TRM process in order to gain the benefits of their basic and redox attributes. In an investigation of La-doping on Ni-CeO<sub>2</sub> catalysts, [Pino et al. \(2011\)](#) reported that CH<sub>4</sub> and CO<sub>2</sub> conversions considerably improved with the addition of 10 wt% La, from 93% to 96% and 83% to 86.5%, respectively, with the absence of carbonaceous deposition. Nevertheless, a significant decline in both CO<sub>2</sub> and CH<sub>4</sub> conversions was observed at excessive La loading beyond 10 wt% La while the H<sub>2</sub>/CO ratio appeared to be unaffected at about 1.62–1.65. The strong interaction within the Ni-La<sub>2</sub>O<sub>3</sub>-surface oxygen vacancies of CeO<sub>2</sub> was considered as the driving force for enhancing catalytic activity by improving the dispersion of Ni particles and inducing the formation of Ce<sup>3+</sup> sites. Additionally, La<sub>2</sub>O<sub>3</sub> promotion was able to create a large number of intermediate and strong basic sites, enabling a stronger binding interaction between the catalyst surface and the CO<sub>2</sub> reactant. As a result, the increasing CO<sub>2</sub> adsorption was able to enhance the reforming activity. The promotional effects of CeO<sub>2</sub> and La<sub>2</sub>O<sub>3</sub> addition on the catalytic performance of Ni/Al<sub>2</sub>O<sub>3</sub> catalyst for TRM were also examined by [Solov'ev et al. \(2012\)](#) at various feed compositions and with reaction temperatures of 814–1123 K. They reported that the addition of CeO<sub>2</sub> or La<sub>2</sub>O<sub>3</sub> promoter provided additional pathways for CO<sub>2</sub> activation. Thus, the formation and decomposition of surface carbonates could yield active oxygen species reacting with surface carbon from CH<sub>4</sub> dissociation on Ni metallic phase.

[García-Vargas et al. \(2014\)](#) examined the influence of alkaline (including Na and K) and alkaline earth (namely, Mg and Ca) promoters on the performance of Ni/ $\beta$ -SiC catalyst. Although Na and K metal oxides were reported as appropriate promoters in other reforming processes, these metal oxides were not useful for TRM. This was assigned to their ability to enhance the oxidation rate of  $\beta$ -SiC during calcination to generate an  $\alpha$ -cristobalite form. A similar behavior was also observed for Ca promoter with high loading. However, the promotion of Mg reduced the Ni metal particle size and increased the basicity of the catalyst resulting in increased activity and stability of the Mg-promoted catalyst. The authors also assessed the effect of Mg loading and found that an increase in the Mg/Ni ratio induced a decline in the crystallite size and in the reducibility of NiO particles, most likely due to NiO-MgO solid solution formation.

In order to facilitate the comparison between catalysts and easily identify the influence of support and promoter types on the TRM catalytic performance,

Table 4.12 summarizes the TRM reaction conditions and catalytic performance of various promoted and supported catalysts. The degree of catalyst deactivation is also estimated based on initial and final CH<sub>4</sub> conversions. Additionally, the H<sub>2</sub>/CO ratio is given to justify the suitability of the produced syngas mixture for downstream processing.

### 4.4.3 Tri-reforming of Methane: Kinetic Model

Kinetic studies are generally conducted to determine the most appropriate reaction rate model that is fundamentally derived from mechanistic reaction pathways in order to capture the experimental reactant reaction rate and the product formation rate with the best fit. In comparison with other reforming processes (namely, methane dry reforming and methane steam reforming reactions), kinetic studies of TRM are relatively fewer and TRM kinetic investigations could become an essential focus in the near future. In kinetic studies of Ni catalysts supported on various metal oxides and mixed oxides, Song and Pan (2004) used a simplified power law model (Eq. (4.22)) to capture both the CH<sub>4</sub> and CO<sub>2</sub> reaction rates. In order to simplify the kinetic model for TRM, they kept the partial pressure of CH<sub>4</sub> and O<sub>2</sub> constant. Thus, the effect of the CH<sub>4</sub> and O<sub>2</sub> partial pressures could be incorporated into other associated constants.

$$r_i = A \exp\left(\frac{-E_{\text{app},i}}{RT}\right) (P_{\text{CO}_2})^{\alpha,i} (P_{\text{H}_2\text{O}})^{\beta,i} \quad (4.22)$$

where  $r_i$  is reaction rate of CH<sub>4</sub> or CO<sub>2</sub> while  $A$  and  $E_{\text{app}}$  are the preexponential factor and apparent activation energy, respectively. Reaction orders for CO<sub>2</sub> and H<sub>2</sub>O are  $\alpha$  and  $\beta$  in this order, whereas  $P_{\text{CO}_2}$  and  $P_{\text{H}_2\text{O}}$  are the corresponding partial pressures of CO<sub>2</sub> and H<sub>2</sub>O. The activation energies and reaction orders for CH<sub>4</sub> and CO<sub>2</sub> reaction rates were estimated from Eq. (4.22) for various supported Ni catalysts and are summarized in Table 4.13.

Based on the estimated activation energies and reaction orders in Table 4.13, Song and Pan (2004) deduced that, because the reaction orders with respect to the H<sub>2</sub>O partial pressure for the CO<sub>2</sub> consumption rate were negative for all catalysts, CO<sub>2</sub> and H<sub>2</sub>O could compete with each other to convert CH<sub>4</sub> to CO and H<sub>2</sub>. Thus, increasing  $P_{\text{H}_2\text{O}}$  may result in a reduction in the CO<sub>2</sub> reaction rate. Apart from the competition effect, the presence of the water gas shift reaction during TRM may partially contribute to the decline of the CO<sub>2</sub> reaction rate in a H<sub>2</sub>O-rich reactant mixture.

As seen in Table 4.13, the TRM kinetic investigation shows that for both the CH<sub>4</sub> and CO<sub>2</sub> reaction rates, the reaction orders with respect to the CO<sub>2</sub> and H<sub>2</sub>O partial pressures were observably different for various catalyst types. Additionally, power law models do not actually comply with intrinsically mechanistic reaction pathways, although they are widely employed to sufficiently capture reactant reaction rates in reforming processes to acquire apparent activation

**TABLE 4.12 Bibliographic List for Catalytic Performance of Recently Employed Catalysts in TRM Reaction**

Catalysts	CH <sub>4</sub> /CO <sub>2</sub> / H <sub>2</sub> O/O <sub>2</sub> Ratio	T (K)	GHSV (L g <sub>cat</sub> <sup>-1</sup> h <sup>-1</sup> )	Initial Performance			TOS <sup>a</sup> (h)	Final Performance			D <sup>b</sup> (%)	References
				CH <sub>4</sub> Conversion (%)	CO <sub>2</sub> Conversion (%)	H <sub>2</sub> / CO Ratio		CH <sub>4</sub> Conversion (%)	CO <sub>2</sub> Conversion (%)	H <sub>2</sub> / CO Ratio		
<i>Supported catalysts</i>												
Ni/Al <sub>2</sub> O <sub>3</sub>	1.0/0.9/0.7/0.3	983	40	19.0	–	–	–	–	–	–	–	Solov'ev et al. (2012)
Ni/SiO <sub>2</sub>	1.0/0.5/0.5/0.1	823	–	25.3	10.3	3.44	4	23.5	3.9	4.09	7.1	Majewski and Wood (2014)
Ni/β-SiC	1.0/0.5/0.5/0.1	1073	60	87.1	29.8	2.00	24	75.2	22.8	2.06	13.7	García- Vargas et al. (2014)
NiMoC	1.0/0.4/0.3/0.2	1073	46	97.0	99.9	–	–	–	–	–	–	Zou et al. (2016)
Ni/ZrO <sub>2</sub> <sup>HfC</sup>	5.0/1.0/2.1/1.0	1073	80	97.9	98.5	–	25	96.4	96.9	–	1.5	Singha et al. (2016)
Ni/ZrO <sub>2</sub> <sup>ImpPd</sup>	5.0/1.0/2.1/1.0	1073	80	92.7	94.2	–	25	14.5	17.7	–	84.4	Singha et al. (2016)
Ni/ZrO <sub>2</sub> <sup>ImpCome</sup>	5.0/1.0/2.1/1.0	1073	80	52.3	42.3	–	25	23.5	20.6	–	7.1	Singha et al. (2016)

Ni/ Mg <sub>0.5</sub> TiO <sub>0.5</sub> O	1.0/0.5/0.5/0.1	1123	–	98.0	82.3	–	50	93.6	79.4	–	4.5	Jiang et al. (2007)
Ni/ Mg <sub>0.75</sub> TiO <sub>0.25</sub> O	1.0/0.5/0.5/0.1	1123	–	86.7	65.2	–	50	84.1	62.3	–	3.0	Jiang et al. (2007)
Ni-Mg/ Ce <sub>0.6</sub> Zr <sub>0.4</sub> O <sub>2</sub>	1.0/0.7/0.5/0.2	1073	61	99.6	65.6	2.20	4	–	–	–	–	Walker et al. (2012)
<i>Promoted catalysts</i>												
La-Ni/Al <sub>2</sub> O <sub>3</sub>	1.0/0.6/1.0/0.2	998	40	100.0	46.0	2.06	–	–	–	–	–	Solov'ev et al. (2012)
Ce-Ni/Al <sub>2</sub> O <sub>3</sub>	1.0/0.7/0.7/0.2	978	40	99.0	43.0	1.83	–	–	–	–	–	Solov'ev et al. (2012)
Ca-Ni/ $\beta$ -SiC	1.0/0.5/0.5/0.1	1073	60	81.1	12.0	2.56	24	72.8	7.0	2.75	11.0	García- Vargas et al. (2014)
Mg-Ni/ $\beta$ -SiC	1.0/0.5/0.5/0.1	1073	60	91.2	35.2	1.88	24	88.7	26.5	2.10	2.7	García- Vargas et al. (2014)
Mg-NiMoC	1.0/0.4/0.3/0.2	1073	46	89.9	84.2	–	–	–	–	–	–	Zou et al. (2016)
K-NiMoC	1.0/0.4/0.3/0.2	1073	46	18.0	0.5	–	–	–	–	–	–	Zou et al. (2016)
Co-NiMoC	1.0/0.4/0.3/0.2	1073	46	93.7	99.9	–	–	–	–	–	–	Zou et al. (2016)

*Continued*

**TABLE 4.12 Bibliographic List for Catalytic Performance of Recently Employed Catalysts in TRM Reaction — cont'd**

Catalysts	CH <sub>4</sub> /CO <sub>2</sub> / H <sub>2</sub> O/O <sub>2</sub> Ratio	T (K)	GHSV (L g <sub>cat</sub> <sup>-1</sup> h <sup>-1</sup> )	Initial Performance			TOS (h)	Final Performance			References
				CH <sub>4</sub> Conversion (%)	CO <sub>2</sub> Conversion (%)	H <sub>2</sub> / CO Ratio		CH <sub>4</sub> Conversion (%)	CO <sub>2</sub> Conversion (%)	H <sub>2</sub> / CO Ratio	
Ce-NiMoC	1.0/0.4/0.3/0.2	1073	46	92.9	99.9	–	–	–	–	–	Zou et al. (2016)
La-NiMoC	1.0/0.4/0.3/0.2	1073	46	93.8	88.0	–	–	–	–	–	Zou et al. (2016)

<sup>a</sup>Time-on-stream (TOS) is defined as the period of stability measurements at a fixed reaction temperature.

<sup>b</sup>Degree of catalyst deactivation, D (%) =  $[1 - (\text{Final CH}_4 \text{ conversion} / \text{Initial CH}_4 \text{ conversion})] \times 100\%$ .

<sup>c</sup>Catalyst was prepared via conventional impregnation method.

<sup>d</sup>Catalyst was prepared via hydrothermal synthesis.

<sup>e</sup>Catalyst was prepared via conventional impregnation method using a commercial ZrO<sub>2</sub> support.

**TABLE 4.13** Activation Energies and Reaction Orders for TRM on Different Supported Ni Catalysts (Song and Pan, 2004)

Catalysts	Temperature (K)	Apparent Activation Energy $E_{app}$ (kJ/mol)		Reaction Order			
		CH <sub>4</sub>	CO <sub>2</sub>	CH <sub>4</sub>		CO <sub>2</sub>	
				$\alpha$	$\beta$	$\alpha$	$\beta$
Ni/Al <sub>2</sub> O <sub>3</sub>	1123	69.1	247.0	0.79	-0.06	1.90	-1.57
Ni/MgO	1123	219.6	160.1	-0.87	-0.64	0.53	-2.59
Ni/MgO/CeZrO	1123	67.4	165.7	0.00	0.03	0.98	-1.08

energy and reaction orders. Thus, in order to examine the interaction between CO<sub>2</sub> and the catalyst surface, [Song and Pan \(2004\)](#) used a simplified Langmuir-Hinshelwood model based on the DRM reaction to avoid the complexity of TRM. The mechanistic steps and rate of reaction for this simplified model are summarized in [Table 4.14](#). Based on the derived TRM kinetic model, they reported that the CO<sub>2</sub> adsorption equilibrium constant,  $K_{CO_2}$ , depended strongly on the interaction of CO<sub>2</sub> with the catalyst surface. Because CO<sub>2</sub> interacted strongly with the catalyst surface, molecularly adsorbed CO<sub>2</sub> species became the most abundant reaction intermediates. Thus, most of active sites could be occupied by associatively adsorbed CO<sub>2</sub> species at increasing CO<sub>2</sub> partial pressure, hence leaving fewer available sites for CH<sub>4</sub> adsorption. Therefore, a decline in the CH<sub>4</sub> reaction rate with increased CO<sub>2</sub> partial pressure was observed and the reaction order with respect to CO<sub>2</sub> reactant became negative. However, in the case of weak CO<sub>2</sub> interaction with the catalyst, the opposite results were evident and the reaction order for CO<sub>2</sub> appeared to be positive.

[Maciel et al. \(2010\)](#) carried out a kinetic evaluation of Ni/ $\gamma$ -Al<sub>2</sub>O<sub>3</sub> catalyst for the TRM reaction and proposed a four-step reaction mechanism as summarized in [Table 4.15](#). Step I indicates the overall combined reactions, including

**TABLE 4.14** Reaction Mechanism of TRM Suggested by [Song and Pan \(2004\)](#)

Mechanistic Steps	
Reactant adsorption	$CH_4 + * \xrightleftharpoons{K_{CH_4}} CH_4^*$
	$CO_2 + * \xrightleftharpoons{K_{CO_2}} CO_2^*$
Surface reaction	$CH_4^* + CO_2^* \rightarrow 2H_2 + 2CO + 2^*$
Rate of CH <sub>4</sub> reaction	$-r_{CH_4} = \frac{kK_{CH_4}K_{CO_2}P_{CH_4}P_{CO_2}}{(1 + K_{CH_4}P_{CH_4} + K_{CO_2}P_{CO_2})^2}$

*Note: \* is an available active site on catalyst surface and k is the rate constant of rate-determining step.*

**TABLE 4.15** The Four-Step Reaction Mechanism for the TRM Reaction Proposed by [Maciel et al. \(2010\)](#)

Reaction Steps	Rate Models
Step I: $CH_4 + \frac{5}{8}O_2 \leftrightarrow CO + \frac{7}{4}H_2 + \frac{1}{4}H_2O$	$r_I = \frac{k_1 K_{CH_4} P_{CH_4} K_{O_2} P_{O_2}}{(1 + K_{CH_4} P_{CH_4} + K_{O_2} P_{O_2})^2}$
Step II: CH <sub>4</sub> cracking $CH_4 \rightarrow C + 2H_2$	$r_{II} = \frac{k_2 K_{CH_4} P_{CH_4}}{1 + K_{CH_4} P_{CH_4}}$
Step III: Boudouard reaction $2CO \rightarrow C + CO_2$	$r_{III} = k_3 P_{CO}^2$
Step IV: Reverse water gas-shift reaction $CO_2 + H_2 \rightarrow CO + H_2O$	$r_{IV} = k_4 \left( P_{H_2} P_{CO_2} - \frac{P_{CO} P_{H_2O}}{K_{eq}} \right)$

methane dry reforming, methane steam reforming, methane partial oxidation, and methane oxidation, whereas step II is the methane cracking reaction to form solid carbon and H<sub>2</sub>. Besides these main reactions, the Boudouard reaction and the reverse water gas-shift reaction were also considered in the corresponding steps III and IV. Based on the rate laws of the four-step TRM reaction mechanism, the reactant consumption rate ( $-r_{\text{CH}_4}$  and  $-r_{\text{CO}_2}$ ) and the product formation rate ( $r_{\text{H}_2}$  and  $r_{\text{CO}}$ ) were expressed as follows:  $-r_{\text{CH}_4} = -r_{\text{I}} - r_{\text{II}}$ ;  $-r_{\text{CO}_2} = r_{\text{III}} - r_{\text{IV}}$ ;  $r_{\text{H}_2} = (7r_{\text{I}}/4) + 2r_{\text{II}} - r_{\text{IV}}$ ; and  $r_{\text{CO}} = r_{\text{I}} - 2r_{\text{III}} + r_{\text{IV}}$ . By evaluating the TRM kinetic model, the authors deduced that methane decomposition yielded carbon deposition and hydrogen during the TRM reaction while the high CO production rate was attributed to the concomitant presence of the reverse water gas-shift reaction and carbon gasification by carbon dioxide and oxygen reactants.

[Garcia-Vargas et al. \(2015\)](#) examined the effect of temperature and feed composition on the catalytic behavior of Ni-Mg/ $\beta$ -SiC catalyst for the TRM reaction. They observed that oxygen was not virtually detected in the effluent stream from the outlet of the reactor, indicating that methane partial oxidation rapidly achieved full conversion during the TRM process. Thus, experimental data were simply fitted to kinetic expressions for individual reactions, including methane steam reforming, methane dry reforming, and water gas-shift reaction. In fact, kinetic equations proposed by [Wei and Iglesia \(2004a, b\)](#) and [De la Osa et al. \(2011\)](#) for the corresponding reforming reactions (namely, steam and DRM) and water gas-shift reaction were employed for assessing the fitness of the experimental reaction rates of the TRM reaction.

[Table 4.16](#) summarizes the reaction rates and associated kinetic parameters involved in the TRM reaction from the findings of [Garcia-Vargas et al. \(2015\)](#). In that study, the kinetic parameters were estimated using the Arrhenius' equation,  $k_i = k_i^0 e^{(-E_{a,i}/RT)}$  with  $k_i^0$ ,  $E_{a,i}$ ,  $R$ , and  $T$  being the corresponding preexponential factor for reaction  $i$ , activation energy, the universal gas constant, and the reaction temperature. A good agreement was obtained between the modeled results and the experimental data, with average errors of 10.8% and 19.4% for CH<sub>4</sub> and CO<sub>2</sub> molar flows, respectively. Additionally, the estimated activation energies (see [Table 4.16](#)) for each main reaction during the TRM process were consistent with the range of values reported in the literature for steam reforming and DRM ([Garcia-Vargas et al., 2015](#)).

#### 4.4.4 Conclusions and Outlook

The catalytic TRM process appears to be a promising substitution for other conventional reforming processes for syngas production at an industrial scale as it is a synergistic combination of methane steam reforming, methane dry reforming, and methane partial oxidation. Particularly, coupling methane dry reforming and methane steam reforming can provide the flexible tuning of H<sub>2</sub>/CO ratios by adjusting the reactant feed composition, while the simultaneous presence of

**TABLE 4.16** Kinetic Expressions and Associated Parameters for Each Reaction Involved in the TRM Process (Garcia-Vargas et al., 2015)

Rate Models	Associated Kinetic Parameters
<p>For methane steam reforming:</p> $r_{SR} = k_1 P_{CH_4} \left( 1 - \frac{P_{CO} P_{H_2}^3}{P_{CH_4} P_{H_2O} K_{SR}} \right)$ $K_{SR} = 1.198 \times 10^{17} e^{\left( \frac{-26830}{T} \right)}$	$k_1^0 = 85.77 \text{ mol s}^{-1} \text{ kPa}^{-1}$ $E_{a_1} = 74.72 \text{ kJ mol}^{-1}$
<p>For methane dry reforming:</p> $r_{DR} = k_2 P_{CH_4} \left( 1 - \frac{P_{CO}^2 P_{H_2}^2}{P_{CH_4} P_{CO_2} K_{DR}} \right)$ $K_{DR} = 6.780 \times 10^{18} e^{\left( \frac{-31230}{T} \right)}$	$k_2^0 = 70.99 \text{ mol s}^{-1} \text{ kPa}^{-1}$ $E_{a_2} = 77.82 \text{ kJ mol}^{-1}$
<p>For water gas-shift reaction:</p> $r_{WGS} = k_3 \left( \frac{P_{CO} P_{H_2O}}{P_{H_2}} - \frac{P_{CO_2}}{K_{WGS}} \right)$ $K_{WGS} = 10^{\left( \frac{2078}{T} - 2.029 \right)}$	$k_3^0 = 149.92 \text{ mol s}^{-1} \text{ kPa}^{-1}$ $E_{a_3} = 54.26 \text{ kJ mol}^{-1}$

H<sub>2</sub>O, CO<sub>2</sub>, and O<sub>2</sub> oxidizing agents in the TRM reaction substantially reduce coke formation, and hence enhance the catalytic activity and prolong the catalytic lifespan.

However, bibliographic knowledge about the TRM reaction is still little-known in both academic and industrial realms due to the complexity of this reaction. Additionally, catalyst deactivation caused by carbonaceous deposition as well as thermal sintering is always an unavoidable problem of reforming processes. Hence, studies related to carbon-resistant catalyst development have been extensively conducted by employing different groups of metals and supports to examine their synergetic effect on catalytic performance and stability over the TRM reaction.

Additionally, the use of advanced catalyst preparation approaches in order to maximize the combined benefits of promoters and supports could substantially affect the physicochemical attributes of catalysts, namely, the extent of interaction between metal and support, as well as surface metal dispersion. In order to effectively design a functional catalyst and optimize reactor design, the best-fit kinetic modeling derived from the intrinsic TRM mechanistic steps is crucial. Hence, future research on adequate catalyst synthesis methods and TRM kinetics should be considered to improve catalytic performance and stability for the industrial application of the TRM process.

## 4.5 GENERAL CONCLUSIONS

At the present time, SMR is still the predominant process for hydrogen production from fossil resources. However, green hydrogen can be obtained from biogas as a renewable resource using not only SMR but also dry, dual, and tri-reforming processes. These alternative solutions have the advantages of employing carbon dioxide, a major component of biogas, as an oxidant in the reforming reaction, and also minimizing the steam to carbon (S/C) ratio compared to actual SMR processes. However, catalyst deactivation is still identified as the main drawback for the deployment of these reforming technologies. Among numerous studies on the catalysts for dry, dual, and tri-reforming of methane, some of them showed very promising catalytic performance. The thermodynamic equilibrium, reaction pathway and kinetic of these reforming processes are discussed in this chapter. Significant progress has been made recently but effort is still needed to determine most kinetic and mechanistic aspects of these processes.

## ACKNOWLEDGMENTS

This work is a part of the *VABHYOGAZ3* project supported by the French “*Programme d’Investissements d’Avenir*” under the supervision of *ADEME*, the French Energy and Environment Agency. The authors are grateful to the *ADEME* for its support for this project. This work is also the result of the collaboration between “Université de Toulouse, IMT Mines Albi, UMR CNRS 5302, Centre RAPSODEE,” “Faculty of Chemical and Natural Resources Engineering, University Malaysia Pahang,” and HERA-ALBHYON enterprise.

## REFERENCES

- Abbas, S.Z., Dupont, V., Mahmud, T., 2017. Kinetics study and modelling of steam methane reforming process over a NiO/Al<sub>2</sub>O<sub>3</sub> catalyst in an adiabatic packed bed reactor. *Int. J. Hydrog. Energy* 42, 2889–2903.
- Abdollahifar, M., Haghghi, M., Babaluo, A.A., Talkhoncheg, S.K., 2016. Sono-synthesis and characterization of bimetallic Ni-Co/Al<sub>2</sub>O<sub>3</sub>-MgO nanocatalyst: effects of metal content on catalytic properties and activity for hydrogen production via CO<sub>2</sub> reforming of CH<sub>4</sub>. *Ultrason. Sonochem.* 31, 173–183.
- Abdullah, B., Ghani, N.A.A., Vo, D.-V.N., 2017. Recent advances in dry reforming of methane over Ni-based catalysts. *J. Clean. Prod.* 162, 170–185.
- ADEME (2014a) *Climat, Air, Energie*.
- ADEME (2014b) *Alléger l’empreinte environnementale de la consommation des Français en 2030. Rapport de synthèse*.
- Air Liquide, n.d. <https://www.engineering-airliquide.com/fr/reformage-du-methane-vapeur-production-dhydrogene> (Accessed on May 16, 2018).
- Akbari, E., Alavi, S.M., Rezaei, M., 2017. Synthesis gas production over highly active and stable nanostructured Ni-MgO-Al<sub>2</sub>O<sub>3</sub> catalysts in dry reforming of methane: effects of Ni contents. *Fuel* 194, 171–179.

- Albarazi, A., Beaunier, P., Da Costa, P., 2013. Hydrogen and syngas production by methane dry reforming on SBA-15 supported nickel catalysts: on the effect of promotion by  $\text{Ce}_{0.75}\text{Zr}_{0.25}\text{O}_2$  mixed oxide. *Int. J. Hydrog. Energy* 38 (1), 127–139.
- Al-Fatesh, A.S., 2017. Promotional effect of Gd over  $\text{Ni}/\text{Y}_2\text{O}_3$  catalyst used in dry reforming of  $\text{CH}_4$  for  $\text{H}_2$  production. *Int. J. Hydrog. Energy* 42 (30), 18805–18816.
- Angeli, S.D., Monteleone, G., Giaconia, A., Lemonidou, A.A., 2014. State-of-the-art catalysts for  $\text{CH}_4$  steam reforming at low temperature. *Int. J. Hydrog. Energy* 39, 1979–1997.
- Arandiyán, H., Peng, Y., Liu, C., Chang, H., Li, J., 2014. Effects of noble metals doped on mesoporous  $\text{LaAlNi}$  mixed oxide catalyst and identification of carbon deposit for reforming  $\text{CH}_4$  with  $\text{CO}_2$ . *J. Chem. Technol. Biotechnol.* 89 (3), 372–381.
- Argyle, M.D., Bartholomew, C.H., 2015. Heterogeneous catalyst deactivation and regeneration: a review. *Catalysts* 5 (1), 145–269.
- Ay, H., Üner, D., 2015. Dry reforming of methane over  $\text{CeO}_2$  supported Ni, Co and Ni-Co catalysts. *Appl. Catal. B Environ.* 179, 128–138.
- Ayodele, B.V., Khan, M.R., Lam, S.S., Cheng, C.K., 2016. Production of CO-rich hydrogen from methane dry reforming over lanthania-supported cobalt catalyst: kinetic and mechanistic studies. *Int. J. Hydrog. Energy* 41 (8), 4603–4615.
- Ayodele, B.V., Khan, M.R., Cheng, C.K., 2017. Greenhouse gases abatement by catalytic dry reforming of methane to syngas over samarium oxide-supported cobalt catalyst. *Int. J. Environ. Sci. Technol.* 14 (12), 2769–2782.
- Barroso-Quiroga, M.M., Castro-Luna, A.E., 2007. Kinetic analysis of rate data for dry reforming of methane. *Ind. Eng. Chem. Res.* 46, 5265–5270.
- Barroso-Quiroga, M.M., Castro-Luna, A.E., 2010. Catalytic activity and effect of modifiers on Ni-based catalysts for the dry reforming of methane. *Int. J. Hydrog. Energy* 35 (11), 6052–6056.
- Baysal, M., Gunay, M.E., Yildirim, R., 2017. Decision tree analysis of past publications on catalytic steam reforming to develop heuristics for high performance: a statistical review. *Int. J. Hydrog. Energy* 42, 243–254.
- Bellido, J.D.A., Assaf, E.M., 2009. Effect of the  $\text{Y}_2\text{O}_3\text{-ZrO}_2$  support composition on nickel catalyst evaluated in dry reforming of methane. *Appl. Catal. A Gen.* 352, 179–187.
- Cai, W., Ye, L., Zhang, L., Ren, Y., Yue, B., Chen, X., He, H., 2014. Highly dispersed nickel-containing mesoporous silica with superior stability in carbon dioxide reforming of methane: the effect of anchoring. *Mater.* 7 (3), 2340–2355.
- Cao, Y., Li, H., Zhang, J., Shi, L., Zhang, D., 2016. Promotional effects of rare earth elements (Sc, Y, Ce, and Pr) on  $\text{NiMgAl}$  catalysts for dry reforming of methane. *RSC Adv.* 6 (113), 112215–112225.
- Charisiou, N.D., Siakavelas, G., Papageridis, K.N., Baklavaridis, A., Tzounis, L., Avraam, D.G., Goula, M.A., 2016. Syngas production via the biogas dry reforming reaction over nickel supported on modified with  $\text{CeO}_2$  and/or  $\text{La}_2\text{O}_3$  alumina catalysts. *J. Nat. Gas Sci. Eng.* 31, 164–183.
- Chen, W.H., Lin, M.R., Jiang, T.L., Chen, M.H., 2008. Modeling and simulation of hydrogen generation from high-temperature and low-temperature water gas shift reactions. *Int. J. Hydrog. Energy* 33, 6644–6656.
- De la Osa, A.R., De Lucas, A., Romero, A., Valverde, J.L., Sánchez, P., 2011. Kinetic models discrimination for the high pressure WGS reaction over a commercial CoMo catalyst. *Int. J. Hydrog. Energy* 36 (16), 9673–9684.
- Djinović, P., Pintar, A., 2017. Stable and selective syngas production from dry  $\text{CH}_4\text{-CO}_2$  streams over supported bimetallic transition metal catalysts. *Appl. Catal. B Environ.* 206, 675–682.
- Factsage, n.d., <http://www.factsage.com/> (Accessed on May 16, 2018).

- Ferreira-Aparicio, P., Benito, M.J., 2005. New trends in reforming technologies: from hydrogen industrial plants to multifuel microreformers. *Catal. Rev.* 47, 491–588.
- Foo, S.Y., Cheng, C.K., Nguyen, T.H., Adesina, A.A., 2011. Kinetic study of methane CO<sub>2</sub> reforming on Co-Ni/Al<sub>2</sub>O<sub>3</sub> and Ce-Co-Ni/Al<sub>2</sub>O<sub>3</sub> catalysts. *Catal. Today* 164 (1), 221–226.
- Fouskas, A., Kollia, M., Kambolis, A., Papadopoulou, C., Matralis, H., 2014. Boron-modified Ni/Al<sub>2</sub>O<sub>3</sub> catalysts for reduced carbon deposition during dry reforming of methane. *Appl. Catal. A Gen.* 474, 125–134.
- Fu, X., Su, H., Yin, W., Huang, Y., Gu, X., 2017. Bimetallic molybdenum nitride Co<sub>3</sub>Mo<sub>3</sub>N: a new promising catalyst for CO<sub>2</sub> reforming of methane. *Cat. Sci. Technol.* 7 (8), 1671–1678.
- García-Vargas, J.M., Valverde, J.L., Dorado, F., Sánchez, P., 2014. Influence of the support on the catalytic behaviour of Ni catalysts for the dry reforming reaction and the tri-reforming process. *J. Mol. Catal. A Chem.* 395, 108–116.
- García-Vargas, J.M., Valverde, J.L., Diez, J., Dorado, F., Sanchez, P., 2015. Catalytic and kinetic analysis of the methane tri-reforming over a Ni-Mg/β-SiC catalyst. *Int. J. Hydrog. Energy* 40, 8677–8687.
- Gould, T.D., Montemore, M.M., Lubers, A.M., Ellis, L.D., Weimer, A.W., Falconer, J.L., Medlin, J.W., 2015. Enhanced dry reforming of methane on Ni and Ni-Pt catalysts synthesized by atomic layer deposition. *Appl. Catal. A Gen.* 492, 107–116.
- Habibi, N., Wang, Y., Arandiyán, H., Rezaei, M., 2016. Biogas reforming for hydrogen production: a new path to high-performance of Ni/MgAl<sub>2</sub>O<sub>4</sub> spinel catalysts. *ChemCatChem* 8 (23), 3600–3610.
- Habibi, N., Wang, Y., Arandiyán, H., Rezaei, M., 2017. Effect of substitution by Ni in MgAl<sub>2</sub>O<sub>4</sub> spinel for biogas dry reforming. *Int. J. Hydrog. Energy* 42 (38), 24159–24168.
- IEA, 2009. IEA bioenergy, task 37-energy from biogas and landfill gas. 2009.
- IEA, 2017. IEA, renewables 2017, analysis and forecasts to 2022. 2017.
- Jabbour, K., El Hassan, N., Casale, S., Estephane, J., El Zakhem, H., 2014. Promotional effect of Ru on the activity and stability of Co/SBA-15 catalysts in dry reforming of methane. *Int. J. Hydrog. Energy* 39 (15), 7780–7787.
- Jiang, H., Li, H., Xu, H., Zhang, Y., 2007. Preparation of Ni/Mg<sub>x</sub>Ti<sub>1-x</sub>O catalysts and investigation on their stability in tri-reforming of methane. *Fuel Process. Technol.* 88 (10), 988–995.
- Jones, G., Jakobsen, J.G., Shim, S.S., Kleis, J., Andersson, M.P., Rossmesl, J., Abild-Pedersen, F., Bligaard, T., Helveg, S., Hinnemann, B., Rostrup-Nielsen, J.R., 2008. First principles calculations and experimental insight into methane steam reforming over transition metal catalysts. *J. Catal.* 259 (1), 147–160.
- Kathiraser, Y., Oemar, U., Saw, E.T., Li, Z., Kawi, S., 2015. Kinetic and mechanistic aspects for CO<sub>2</sub> reforming of methane over Ni based catalysts. *Chem. Eng. J.* 278, 62–78.
- LeValley, T.L., Richard, A.R., Fan, M., 2014. The progress in water gas shift and steam reforming hydrogen production technologies—a review. *Int. J. Hydrog. Energy* 39, 16983–17000.
- Li, X., Li, D., Tian, H., Zeng, L., Zhao, Z.J., Gong, J., 2017. Dry reforming of methane over Ni/La<sub>2</sub>O<sub>3</sub> nanorod catalysts with stabilized Ni nanoparticles. *Appl. Catal. B Environ.* 202, 683–694.
- Lide, D.R., 2003–2004. *Handbook of Chemistry and Physics*, 84th ed. CRC Press, Boca Raton, FL.
- Linde. n.d. [http://www.lindeengineering.in/en/process\\_plants/hydrogen\\_and\\_synthesis\\_gas\\_plants/gas\\_products/hydrogen/index.html](http://www.lindeengineering.in/en/process_plants/hydrogen_and_synthesis_gas_plants/gas_products/hydrogen/index.html) (Accessed on May 16, 2018).
- Liu, K., Song, C., Subramani, V., 2010. *Hydrogen and Syngas Production and Purification Technologies*. John Wiley & Sons, Inc., Hoboken, New Jersey.
- Lou, Y., Steib, M., Zhang, Q., Tiefenbacher, K., Horváth, A., Jentys, A., Liu, Y., Lercher, J.A., 2017. Design of stable Ni/ZrO<sub>2</sub> catalysts for dry reforming of methane. *J. Catal.* 356, 147–156.

- Ma, Q., Sun, J., Gao, X., Zhang, J., Zhao, T., Yoneyama, Y., Tsubaki, N., 2016. Ordered mesoporous alumina-supported bimetallic Pd-Ni catalysts for methane dry reforming reaction. *Cat. Sci. Technol.* 6 (17), 6542–6550.
- Maciel, L.J., de Souza, A.E., Cavalcanti-Filho, V.O., Knoechelmann, A., de Abreu, C.A., 2010. Kinetic evaluation of the tri-reforming process of methane for syngas production. *React. Kinet. Mech. Catal.* 101 (2), 407–416.
- Mahoney, E.G., Pusel, J.M., Stagg-Williams, S.M., Faraji, S., 2014. The effects of Pt addition to supported Ni catalysts on dry (CO<sub>2</sub>) reforming of methane to syngas. *J. CO<sub>2</sub> Util.* 6, 40–44.
- Majewski, A.J., Wood, J., 2014. Tri-reforming of methane over Ni@SiO<sub>2</sub> catalyst. *Int. J. Hydrog. Energy* 39 (24), 12578–12585.
- Nguyen, V.N., Blum, L., Peters, R., 2014. Operational behavior and reforming kinetics over Ni/YSZ of a planar type pre-reformer for SOFC systems. *Int. J. Hydrog. Energy* 39, 7131–7141.
- Nguyen, V.N., Deja, R., Peters, R., Blum, L., 2016. Methane/steam global reforming kinetics over the Ni/YSZ of planar pre-reformers for SOFC systems. *Chem. Eng. J.* 292, 113–122.
- Omogbe, O., Danh, H.T., Abidin, S.Z., Setiabudi, H.D., Abdullah, B., Vu, K.B., Vo, D.-V.N., 2016. Influence of lanthanide promoters on Ni/SBA-15 catalysts for syngas production by methane dry reforming. *Procedia Eng.* 148, 1388–1395.
- Omogbe, O., Danh, H., Nguyen-Huy, C., Setiabudi, H., Abidin, S., Truong, Q., Vo, D.-V.N., 2017. Syngas production from methane dry reforming over Ni/SBA-15 catalyst: effect of operating parameters. *Int. J. Hydrog. Energy* 42 (16), 11283–11294.
- Osazuwa, O.U., Setiabudi, H.D., Abdullah, S., Cheng, C.K., 2017. Syngas production from methane dry reforming over SmCoO<sub>3</sub> perovskite catalyst: kinetics and mechanistic studies. *Int. J. Hydrog. Energy* 42 (15), 9707–9721.
- Özkara-Aydinoğlu, Ş., Aksoylu, A.E., 2013. A comparative study on the kinetics of carbon dioxide reforming of methane over Pt-Ni/Al<sub>2</sub>O<sub>3</sub> catalyst: effect of Pt/Ni ratio. *Chem. Eng. J.* 215, 542–549.
- Pakhare, D., Spivey, J., 2014. A review of dry (CO<sub>2</sub>) reforming of methane over noble metal catalysts. *Chem. Soc. Rev.* 43 (22), 7813–7837.
- Pechimuthu, N.A., Pant, K.K., Dhingra, S.C., Bhalla, R., 2006. Characterization and activity of K, CeO<sub>2</sub>, and Mn promoted Ni/Al<sub>2</sub>O<sub>3</sub> catalysts for carbon dioxide reforming of methane. *Ind. Eng. Chem. Res.* 45 (22), 7435–7443.
- Pichas, C., Pomonis, P., Petrakis, D., Ladavos, A., 2010. Kinetic study of the catalytic dry reforming of CH<sub>4</sub> with CO<sub>2</sub> over La<sub>2-x</sub>Sr<sub>x</sub>NiO<sub>4</sub> perovskite-type oxides. *Appl. Catal. A Gen.* 386 (1), 116–123.
- Pino, L., Vita, A., Cipiti, F., Laganà, M., Recupero, V., 2011. Hydrogen production by methane tri-reforming process over Ni-ceria catalysts: effect of La-doping. *Appl. Catal. B Environ.* 104, 64–73.
- Pino, L., Vita, A., Laganà, M., Recupero, V., 2014. Hydrogen from biogas: catalytic tri-reforming process with Ni/LaCeO mixed oxides. *Appl. Catal. B Environ.* 148, 91–105.
- Qian, L., Ma, Z., Ren, Y., Shi, H., Yue, B., Feng, S., Xie, S., 2014. Investigation of La promotion mechanism on Ni/SBA-15 catalysts in CH<sub>4</sub> reforming with CO<sub>2</sub>. *Fuel* 122, 47–53.31.
- Ray, K., Sengupta, S., Deo, G., 2017. Reforming and cracking of CH<sub>4</sub> over Al<sub>2</sub>O<sub>3</sub> supported Ni, Ni-Fe and Ni-Co catalysts. *Fuel Process. Technol.* 156, 195–203.
- Rong-jun, Z., Guo-fu, X., Ming-feng, L., Yu, W., Hong, N., Da-dong, L., 2015. Effect of support on the performance of Ni-based catalyst in methane dry reforming. *J. Fuel Chem. Technol.* 43 (11), 1359–1365.
- Rostrup-Nielsen, J.R., 2002. Syngas in perspective. *Catal. Today* 71, 243–247.

- Sarkar, B., Goyal, R., Pendem, C., Sasaki, T., Bal, R., 2016. Highly nanodispersed Gd-doped Ni/ZSM-5 catalyst for enhanced carbon-resistant dry reforming of methane. *J. Mol. Catal. A Chem.* 424, 17–26.
- Selvarajah, K., Phuc, N.H.H., Abdullah, B., Alenazey, F., Vo, D.-V.N., 2016. Syngas production from methane dry reforming over Ni/Al<sub>2</sub>O<sub>3</sub> catalyst. *Res. Chem. Intermed.* 42 (1), 269–288.
- Shah, Y.T., 2017. *Chemical Energy from Natural and Synthetic Gas*. CRC Press, Boca Raton, FL.
- Shamskar, F.R., Meshkani, F., Rezaei, M., 2017. Preparation and characterization of ultrasound-assisted co-precipitated nanocrystalline La-, Ce-, Zr-promoted Ni-Al<sub>2</sub>O<sub>3</sub> catalysts for dry reforming reaction. *J. CO<sub>2</sub> Util.* 22, 124–134.
- Singh, S.A., Madras, G., 2016. Sonochemical synthesis of Pt, Ru doped TiO<sub>2</sub> for methane reforming. *Appl. Catal. A Gen.* 518, 102–114.
- Singha, R.K., Das, S., Pandey, M., Kumar, S., Bal, R., Bordoloi, A., 2016. Ni nanocluster on modified CeO<sub>2</sub>-ZrO<sub>2</sub> nanoporous composite for tri-reforming of methane. *Cat. Sci. Technol.* 6 (19), 7122–7136.
- Solov'ev, S.A., Gubareni, Y.V., Kurilets, Y.P., Orlik, S.N., 2012. Tri-reforming of methane on structured Ni-containing catalysts. *Theor. Exp. Chem.* 48 (3), 199–205.
- Song, C., Pan, W., 2004. Tri-reforming of methane: a novel concept for catalytic production of industrially useful synthesis gas with desired H<sub>2</sub>/CO ratios. *Catal. Today* 98 (4), 463–484.
- Soria, M.A., Mateos-Pedrero, C., Marín, P., Ordóñez, S., Guerrero-Ruiz, A., Rodríguez-Ramos, I., 2012. Kinetic analysis of the Ru/SiO<sub>2</sub>-catalyzed low temperature methane steam reforming. *Appl. Catal. A Gen.* 413–414, 366–374.
- Temkin, M.I., 1979. Eley, H.P.D.D., Paul, B.W. (Eds.), *Advances in Catalysis*. Academic Press, New York, pp. 173–291.
- Usman, M., Daud, W.W., Abbas, H.F., 2015. Dry reforming of methane: influence of process parameters—a review. *Renew. Sust. Energ. Rev.* 45, 710–744.
- Walker, D.M., Pettit, S.L., Wolan, J.T., Kuhn, J.N., 2012. Synthesis gas production to desired hydrogen to carbon monoxide ratios by tri-reforming of methane using Ni-MgO-(Ce, Zr)O<sub>2</sub> catalysts. *Appl. Catal. A Gen.* 445, 61–68.
- Wang, C., Zhang, Y., Wang, Y., Zhao, Y., 2017. Comparative studies of non-noble metal modified mesoporous M-Ni-CaO-ZrO<sub>2</sub> (M = Fe, Co, Cu) catalysts for simulated biogas dry reforming. *Chin. J. Chem.* 35 (1), 113–120.
- Wang, N., Yu, X., Wang, Y., Chu, W., Liu, M., 2013. A comparison study on methane dry reforming with carbon dioxide over LaNiO<sub>3</sub> perovskite catalysts supported on mesoporous SBA-15, MCM-41 and silica carrier. *Catal. Today* 212, 98–107.
- Wang, N., Xu, Z., Deng, J., Shen, K., Yu, X., Qian, W., Wei, F., 2014. One-pot synthesis of ordered mesoporous NiCeAl oxide catalysts and a study of their performance in methane dry reforming. *ChemCatChem* 6 (5), 1470–1480.
- Wang, Y., Yao, L., Wang, S., Mao, D., Hu, C., 2018. Low-temperature catalytic CO<sub>2</sub> dry reforming of methane on Ni-based catalysts: a review. *Fuel Process. Technol.* 169, 199–206.
- Wei, J., Iglesia, E., 2004a. Reaction pathways and site requirements for the activation and chemical conversion of methane on Ru-based catalysts. *J. Phys. Chem. B* 108, 7253–7262.
- Wei, J., Iglesia, E., 2004b. Isotopic and kinetic assessment of the mechanism of reactions of CH<sub>4</sub> with CO<sub>2</sub> or H<sub>2</sub>O to form synthesis gas and carbon on nickel catalysts. *J. Catal.* 224 (2), 370–383.
- Xie, T., Zhao, X., Zhang, J., Shi, L., Zhang, D., 2015. Ni nanoparticles immobilized Ce-modified mesoporous silica via a novel sublimation-deposition strategy for catalytic reforming of methane with carbon dioxide. *Int. J. Hydrog. Energy* 40 (31), 9685–9695.

- Xu, J., Froment, G., 1989. Methane steam reforming, methanation and water-gas shift. 1. Intrinsic kinetics. *AICHE J.* 35, 88–96.
- Xu, J., Saeys, M., 2007. First principles study of the coking resistance and the activity of a boron promoted Ni catalyst. *Chem. Eng. Sci.* 62 (18), 5039–5041.
- Yao, L., Galvez, M.E., Hu, C., Da Costa, P., 2017. Mo-promoted Ni/Al<sub>2</sub>O<sub>3</sub> catalyst for dry reforming of methane. *Int. J. Hydrog. Energy* 42 (37), 23500–23507.
- Zarei, M., Meshkani, F., Rezaei, M., 2016. Preparation of mesoporous nanocrystalline Ni-MgAl<sub>2</sub>O<sub>4</sub> catalysts by sol-gel combustion method and its applications in dry reforming reaction. *Adv. Powder Technol.* 27 (5), 1963–1970.
- Zeppieri, M., Villa, P.L., Verdone, N., Scarsella, M., De Filippis, P., 2010. Kinetic of methane steam reforming reaction over nickel- and rhodium-based catalysts. *Appl. Catal. A Gen.* 387, 147–154.
- Zhang, L., Zhang, Q., Liu, Y., Zhang, Y., 2016. Dry reforming of methane over Ni/MgO-Al<sub>2</sub>O<sub>3</sub> catalysts prepared by two-step hydrothermal method. *Appl. Surf. Sci.* 389, 25–33.
- Zhang, S., Muratsugu, S., Ishiguro, N., Tada, M., 2013. Ceria-doped Ni/SBA-16 catalysts for dry reforming of methane. *ACS Catal.* 3 (8), 1855–1864.
- Zhang, S., Shi, C., Chen, B., Zhang, Y., Zhu, Y., Qiu, J., Au, C., 2015. Catalytic role of β-Mo<sub>2</sub>C in DRM catalysts that contain Ni and Mo. *Catal. Today* 258, 676–683.
- Zou, H., Chen, S., Huang, J., Zhao, Z., 2016. Effect of additives on the properties of nickel molybdenum carbides for the tri-reforming of methane. *Int. J. Hydrog. Energy* 41 (38), 16842–16850.